

Master Thesis

**Evaluation, design and realisation of a  
Riemann Pump for the frequency  
range of 0..6 GHz for 5G mobile  
communication**

Markus Weiß

Degree Programme: Embedded Systems Engineering

Matriculation Number: 3728492

Supervisor: Prof. Dr. Oliver Ambacher  
PD Dr. techn. Rüdiger Quay

Period: 01.11.2015 – 02.05.2016

Freiburg, 02.05.2016



# **Declaration**

I hereby declare that this thesis is my own work and effort and that all sources cited or quoted are indicated and acknowledged by means of a comprehensive list of references.

Freiburg, 02.05.2016

Markus Weiß



# Abstract

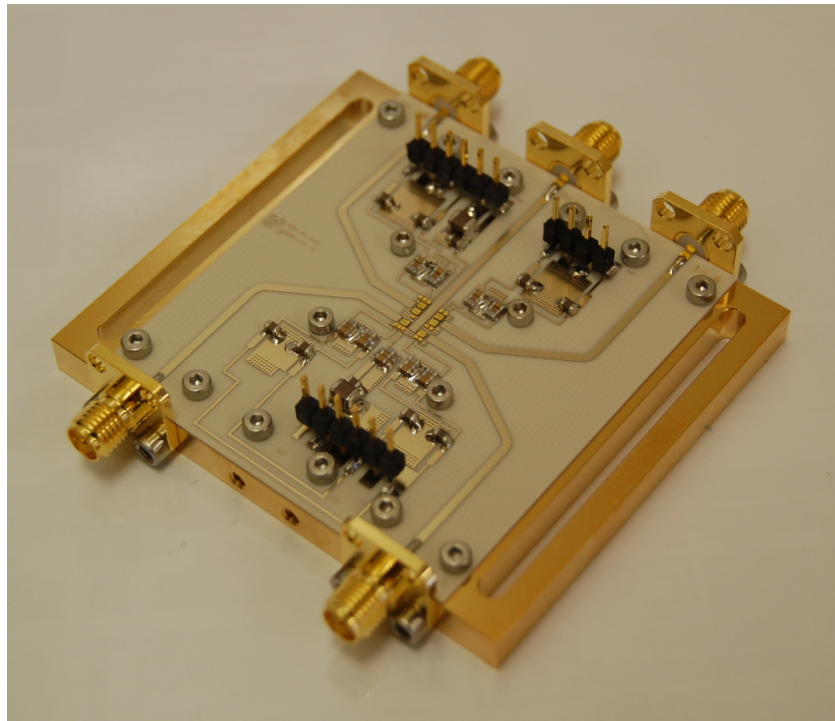


Fig. 0.1.: Built demonstrator

To the best of the author's knowledge, the worldwide first realised Riemann Pump in GaN technology is presented in Figure 0.1.

In this work a new concept of digital to analog conversion is investigated, yielding an arbitrary waveform generator which can be used in the next generation of mobile communication. This waveform generator is able to cover the frequency range from DC to 6 GHz, which simulations confirmed. With the help of this multi bit resolution of a charge pump, the actual conversion methods of digital to analog conversion are enhanced impressively.

The realised hybrid test circuit was designed, implemented and measured to proof the concept of a push-pull stage, functioning as a differential switch, providing a multi bit charge pump. The multi chip solution is chosen to proof the feasibility of the approach and to depict already trade offs which occur during the work.

Although the simulations confirmed the feasibility to cover the broadband frequency

range some practical drawbacks were mentioned, which limit the frequency range. As the generation of the signal wave form at the output of the circuit, generates much heat, two different concepts were demonstrated to deal with the heat spreading. As the energy consumption of modern digital to analog conversions with multi bit resolution is critical an approach is chosen which yields a good efficiency.

# Zusammenfassung

In dieser Arbeit wird ein neues Konzept der Digital-Analog-Umwandlung untersucht, ein Arbitrary Waveform Generator ergibt, die in der nächsten Generation der Mobilkommunikation verwendet werden könnten. auf SI 6 giga Hertz, die bestätigt Simulationen: Diese Wellenform-Generator sollte den Frequenzbereich von gls dc ab abdecken können. Mit Hilfe dieser Multi-Bit-Auflösung einer Ladungspumpe, die tatsächlichen Umrechnungsmethoden Digital-Analog-Umwandlung kann verbessert werden.

Der realisierte Hybrid-Testschaltung wurde entwickelt, umgesetzt und bis zum Beweis das Konzept einer Push-Pull-Stufe gemessen, als Differenzschalter funktioniert, ein Multi-Bit-Ladungspumpe bereitstellt. Die Multi-Chip-Lösung wird die Machbarkeit des Ansatzes zu Beweis gewählt und bereits Kompromisse darstellen, die während der Arbeit auftreten. Obwohl die Simulationen bestätigt die Machbarkeit der Breitband-Frequenzbereich einige praktische Nachteile zu decken erwähnt wurden, die den Frequenzbereich zu begrenzen. Da die Erzeugung des Formsignals Welle am Ausgang der Schaltung, viel Wärme erzeugt, zwei unterschiedliche Konzepte wurden nachgewiesen mit der Wärmeverteilung zu behandeln. Da der Energieverbrauch der modernen Digital-Analog-Umwandlungen mit einer Auflösung Mehrbit ist entscheidend ein Ansatz gewählt, der einen guten Wirkungsgrad liefert.



# Contents

<b>List of abbreviations</b>	<b>iii</b>
<b>List of symbols</b>	<b>v</b>
<b>1. Introduction</b>	<b>1</b>
<b>2. Fundamentals of the Riemann Pump</b>	<b>3</b>
2.1. Basic concept of software-defined radio for 5G mobile communication . . . . .	3
2.2. System design using the Riemann Pump . . . . .	4
2.3. Idea of the Riemann Pump . . . . .	6
2.4. Characteristics of Digital-to-Analog converter . . . . .	9
2.5. Conclusion of the fundamentals . . . . .	11
<b>3. Riemann Pump circuit design</b>	<b>13</b>
3.1. Approach and implementation of the Riemann Pump . . . . .	13
3.2. Identification of the load impedance . . . . .	14
3.3. Dimension of the used components . . . . .	16
3.4. Circuit design summary . . . . .	17
<b>4. Circuit simulations for generating various waveform signals</b>	<b>19</b>
4.1. Generating various analog signals with digital input control . . . . .	19
4.1.1. Sine wave generation in the time domain . . . . .	20
4.1.2. Rectified sine wave generation in the time domain . . . . .	24
4.1.3. Triangular wave generation in the time domain . . . . .	26
4.2. Stability analysis of the realised circuit . . . . .	28
4.3. Energy consumption analysis of the realised circuit . . . . .	28
4.4. Proof of concept simulation with existing components . . . . .	29
4.5. Evaluation of the simulation results for the Riemann Pump . . . . .	29
<b>5. Realisation of a demonstrator</b>	<b>31</b>
5.1. Substrate layout using DDRi_X6 and DDRi_Y6 chips . . . . .	32
5.2. Substrate layout using DDRi_2C chips . . . . .	35
5.3. Evaluation of the design and realisation process . . . . .	36

<b>6. Measurement of the realized circuit in the time domain</b>	<b>39</b>
6.1. Measurement setup . . . . .	39
6.2. Calibration and stability check . . . . .	41
6.3. Time domain measurement of push-pull stage . . . . .	42
6.4. Time domain measurement of synthesized signal . . . . .	43
6.5. Discussion of measurement results . . . . .	44
<b>7. Conclusions and outlook</b>	<b>45</b>
<b>Bibliography</b>	<b>47</b>
<b>Appendix</b>	<b>51</b>
A. Schematic of the Riemann Pump circuit . . . . .	51
B. Layout of the whole Riemann Pump circuit . . . . .	52
C. Photography of the realized Demonstrator version 1 . . . . .	53
D. Photography of the realized Demonstrator version 2 . . . . .	53

# List of abbreviations

ADS	Advanced Design System
Au	Aurum - Gold
AWG	arbitrary waveform generator
ChemNiPdAu	chemical Nickel Palladium Aurum
Cu	Copper
DAC	digital-to-analog converter
DC	direct current
DSP	digital signal processor
DUT	device under test
ESR	equivalent series resistance
GaN	gallium nitride
HEMT	high electron mobility transistor
IAF	Fraunhofer-Institut für Angewandte Festkörperphysik
LNA	low noise amplifier
LTE	Long-Term Evolution
MAG	maximum available gain
MMIC	microwave monolithic integrated circuit
MSL	microstrip line
OSR	oversampling ratio
PCM	Pulse-code modulation
PLL	phase locked loop
RF	radio frequency
RF-FE	radio frequency front-end
SDR	software-defined radio
SMD	surface mounted device
SNR	signal-to-noise-ratio

SQNR signal-to-quantization-noise-ratio

# List of symbols

$C_{out}$	output capacitance
$I_G$	DC-component of the gate current
$V_{dd}$	positive supply voltage
$V_{gs}$	gate source voltage
$V_{out}$	output voltage
$V_{ss}$	negative supply voltage
$f_{Nyquist}$	Nyquist Frequency
$f_{sampling}$	sampling frequency/rate
$f_{signal,max}$	maximum signal frequency
$i_{out}$	output current



# 1. Introduction

## Description of the task.

Mobile communication became a major part of our daily life. With the release of the fourth mobile communication standard LTE (Long-Term Evolution), over seventy 70 power stations are in operation. In our every day life applications such as Instagramm, Whatsapp, facebook and Snapchat are dealing with very high data transfer rates. The industry also handles a very big amount of data. Real time trading at a stock exchange market is crucial, so the industry tries to reach this with the help of RF mobile communication. The data rate is increasing exponentially up to the year 2020. Todays hardware architectures can not handle this amount of data. In the next generation, the fifth, of mobile communication different concepts are needed to deal with this high data rate. In the next generation new hardware architecture are needed. This new concepts are based on the idea of a full software radio. The concept is basically to bring the digital domain as close as possible to the RF Front-End. Therefore the filter, mixer and computation would be much faster, more accurate and less complex.

In Chapter two some fundamentals are explain to get a better understanding of the work. Chapter three explains the design workflow to get to an working principle and a schematic. Chapter four evaluates the principle and after a successful simulation the layout is done in chapter five. after designing and layouting the schematic lastly the measurements are taken. in the end the results are discussed.

5G will be the gamechanger for autonomous driving. low latency (nearly realtime) and super high speed networks. Ten years ago the most shared thing was text, then it becomes pictures and nowadays it is video. But this is not the end of the line, the next step would be a 360 degree angle camera, 3 dimensional, high resolution live stream a la virtual reality. This would mean the next mobile communication standard, 5G, is an enhancement for high data rate and bandwidth and of course the low latency, near to real time transmission. Another topic will be the voice controlled everything, keyword IoT. The smartphone will be overcome with another gadget, most likely voice controlled. This voice control creates a lot more data than tipping it into the keyboard of a smartphone. 5G also means to connect the world, so Mark Zuckerberg. The next standard should be more efficient, cheaper and therefore it should be affordable for every country. Also it could be possible to cover those countries via satellite.



## **2. Fundamentals of the Riemann Pump**

To place this work into the context of the next generation of mobile communication, a concept is described called software-defined radio. Implemented in this concept, the function, the benefit and some fundamentals of the Riemann Pump are described. A demonstrated system shows the SDR (software-defined radio) concept, which is based on the idea to bring the digital domain as close as possible to the antenna. The Riemann Pump is an arbitrary waveform generator which is controlled by a digital input signal, making it also a custom DAC (digital-to-analog converter). The concept of the custom designed DAC as well as some characteristics are presented. A concise discussion conclude the presented fundamentals.

### **2.1. Basic concept of software-defined radio for 5G mobile communication**

The concept of software-defined radio is treated to overcome old problems of mobile communication and hence deal with a fast adapting system which can handle several mobile communication standards at once. New standards can handled since the system can be changed with an firmware update. Therefore every signal within the proposed bandwidth could be processed without changing the hardware, which made it software defined. The ability to process a spectrum of DC (direct current) to 6 GHz enables it to deal with future mobile communication standards.

To achieve this goal it is essential to bring the digital domain as close as possible to the antenna [1], [2],[3]. The digital domain has a lot of advantages regarding complexity, cost, filtering and processing speed [4], [5]. The structure of digital components is less complex and therefore has less cost. Digital filtering is more precisely and data processing is more efficient and faster [6], [7].

The ultimate software defined radio architecture is shown in Figure 2.1.

In this vision the analog received signal is directly converted into the digital domain and afterwards filtered, mixed, demodulated and processed. The absence of the RF-FE (radio frequency front-end) is a dream still to come true [3].

Figure 2.2 shows the feasibility (left) and the estimated power consumption (right), which demonstrates that this vision is not a realistic option.



Fig. 2.1.: Ultimate Software-defined radio architecture [2]



Fig. 2.2.: Feasibility (left) and estimation of energy consumption (right) regarding Effective number of Bits and Sample Rate [3]

In order to reduce the power consumption some analog components like LNA (low noise amplifier), filter, mixer have to be implemented separate in the analog domain for the receiving path. While for the transmitting path, the concept of the Riemann Pump comes into play.

## 2.2. System design using the Riemann Pump

The focus in this thesis was on the transmitting path of the mentioned system, since the receiving architecture and concepts need a separate investigation. Further details on the receiving concepts and investigations can be found in [1], [8], [9], [10]. Since the transmitting path is considered, the need for a DAC becomes visible, as the digital data must be converted to an analog signal before transmission. As mentioned before high demands are made to the DAC implemented in a SDR concept.

An important requirement is to keep the energy consumption in a moderate range. If

the consumed energy is in the range of several kW (Figure 2.2) it is clear that this is unworkable. In order to meet RF (radio frequency) standards the SNR (Signal-to-noise-ratio) has to fulfil the given limits. To achieve a moderate SNR, the resolution and the OSR (oversampling ratio) of the DAC have to meet the requirements. The generated analog output signal, which can consist of a few concurrent signals, has to be amplified for the propagation. To avoid unwanted distortions in the propagated signals linearity of the system is crucial.

Figure 2.3 demonstrates the transmitting path of the system design for the concept of SDR with the implementation of the Riemann Pump.

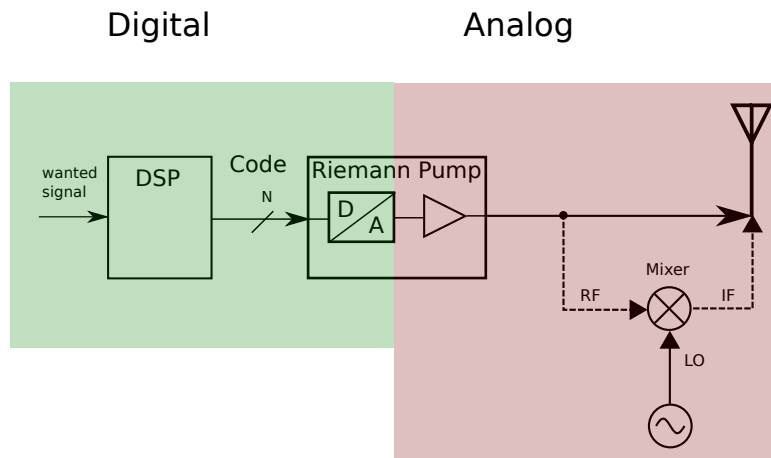


Fig. 2.3.: Concept of the Software-defined radio

The demonstrated path in Figure 2.3 is subdivided into a digital and analog part. The green digital part is responsible for the calculation of the desired signals and the generation of the corresponding digital code. A theoretical wanted signal in the time domain, consisting of multiple modulated signals, is fed to a DSP (digital signal processor) which computes a digital bit-stream. The so called Riemann Code controls the input of a custom DAC, called Riemann Pump, which is the interface between the digital and the analog part.

In the red analog domain the desired signal is amplified by an implemented power transistor in the Riemann Pump and then propagated via the antenna. Optionally a mixer can be connected to mix the desired signal to even higher frequencies of several tenth of GHz.

Beside the advantages of the concept there are some constraints on the energy consumption as well as on the real time emission. Energy consumption is increasing linear with the switching frequency and therefore with the signal bandwidth. Secondly the real time emission is constrained due to the calculation and conversion of the Riemann Code.

## 2.3. Idea of the Riemann Pump

After the implementation in a system design has been demonstrated, the concept of Riemann Pump itself is explained.

The concept shown in Figure 2.4, is implemented in conventional PLLs (phase locked loops) and is known as a charge pump, which is the basic principle of the Riemann Pump [2], [11], [12]. Basically the inputs are switches and the output is a capacitance. The output capacitance ( $C_{out}$ ) can take any value between the positive ( $V_{dd}$ ) and negative ( $V_{ss}$ ) power supply voltage by controlling the input switches.

The integration of the electrical current ( $i_{out}$ ) at the capacitance ( $C_{out}$ ), to form the output voltage ( $V_{out}$ ), recalls the founder of the integration principle, Bernhard Riemann. This integration and the concept of the charge pump lead to the name Riemann Pump, first mentioned in 2013 [2].

Figure 2.4 shows the basic principle of a charge pump, used for the digital to analog conversion in this thesis.

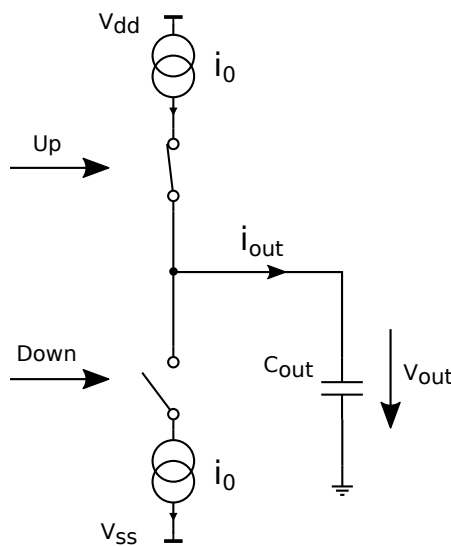


Fig. 2.4.: scheme of a charge pump

Two switches are shown, which are capable to switch current to and from the output capacitance, respectively. The high side switch, which pushes charges onto the output capacitance, is connected to a current source at  $V_{dd}$ . In contrast to that, the low side switch is connected to a current source at  $V_{ss}$ . While controlling the switches with a differential input signal, the output voltage can be varied between  $V_{dd}$  and  $V_{ss}$ . As the control signal only consists of closing and opening a switch, a digital signal is sufficient. If the high side switch is closed while the low side switch is opened, charges are pumped to the capacitance which leads to an increase in output voltage. This effect only takes place if the control

signal is differential, which leads to synchronous switching behaviour of both switches. Otherwise the controlling of the output voltage is not defined. If both switches are closed at the same time, the potential at the capacitor is floating and hence no defined voltage can be stated. For decreasing the output voltage the low side switch has to be closed, while the high side switch is open, to allow the capacitor to discharge.

Corresponding to the described principle, the output voltage

$$V_{out} = \frac{1}{C_{out}} \int_0^T i_{out}(t) dt \quad (2.1)$$

is calculated by integrating the current over time.

A custom DAC is created by extending the basic charge pump with several other charge pumps in parallel, as seen in Figure 2.5. Since the output voltage, consisting of the desired signals, should be propagated via an antenna, the output capacitance  $C_{out}$  can be interpreted as the input stage of a linear power amplifier. This input stage consists of a power transistor, which do have the capacitive input impedance characteristic. Implemented in one component this concept saves area and costs and the amplified signal at the drain can be transmitted via the antenna.

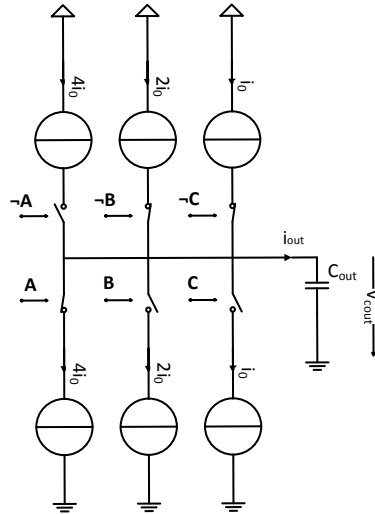


Fig. 2.5.: Concept of the Riemann Pump with three-bit resolution

The dimensions of the current sources, connected in parallel, have to increase by the power of two to get a defined set of currents. Demonstrated is a DAC with three bit resolution, which leads to eight different currents. Instead of using absolute current values, relative currents with respect to  $i_0$  are used. This leads to eight different slopes which are used for the digital to analog conversion process. These eight different slopes are presented in Figure 2.6.

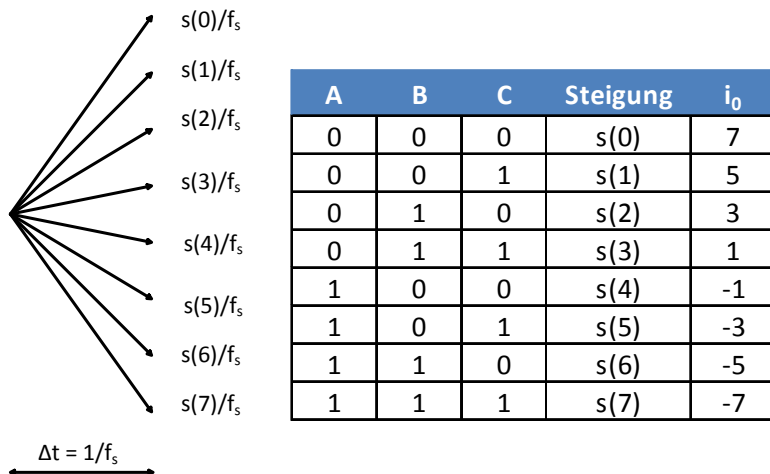


Fig. 2.6.: slopes and corresponding code of the synthesized signal

Corresponding to the demonstrated eight different slopes on the left side, a table is presented which states the corresponding encryption for each slope on the right side. The representation of the relative slope of  $-1i_0$  is:  $100 \equiv s(4)$ . Each digit of the code states the position of the corresponding switches, that is 0 for closed and 1 for an opened switch. Every single charge pump is represented by one bit, making it a three bit resolution in this example. With the help of the encryption table in Figure 2.6 a Riemann Code is generated to synthesize a time domain signal. Figure 2.7 illustrates the generation process of the Riemann Code.

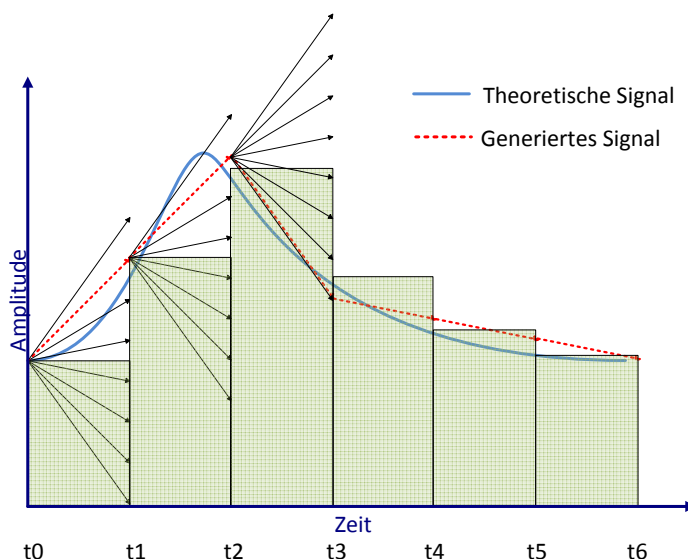


Fig. 2.7.: Integral of the current which pumps charges on to the cap.

The desired signal, consisting of multiple different signals where each can have a different modulation and symbol rate, is pre processed and then sampled with the Riemann Conversion. This theoretically signal is depicted blue. With the aid of the defined set of slopes a signal can be synthesized (red dotted), which yields the Riemann Code. The Code generation is based on minimizing the error between the theoretical signal and the piecewise linear approximation of the signal, created with the different slopes. This minimization is depicted in Figure 2.8.

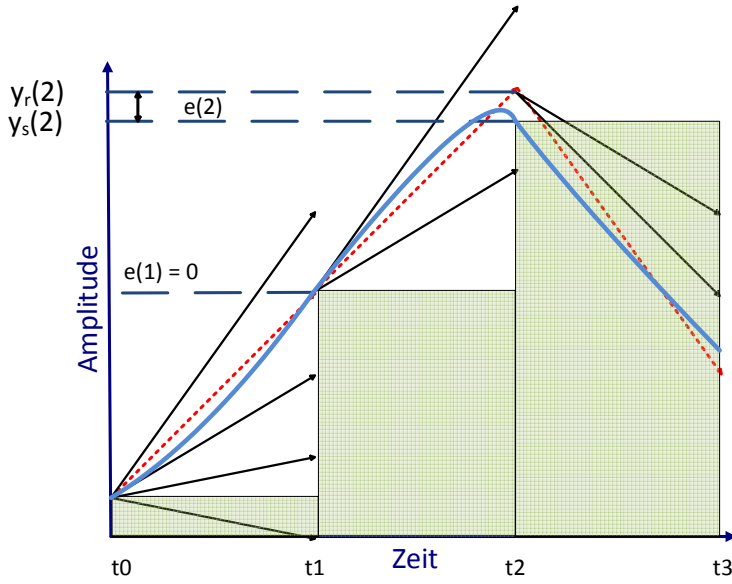


Fig. 2.8.: Code generation - error minimizing

For each sampling point the slope with the smallest deviation in amplitude to the theoretical signal is chosen [11]. This yields a set of slopes representing a Riemann Code for the desired signal. Arbitrary waveforms can be generated using this technique. To avoid unwanted signal clipping it is important that the output capacitance is neither fully charged nor discharged.

## 2.4. Characteristics of Digital-to-Analog converter

To reach modern RF standards, a minimum amount of resolution and oversampling is needed. Oversampling is crucial for the recovery of a signal, due to the Nyquist-Shannon sampling theorem

$$f_{Nyquist} = 2f_{signal,max}. \quad (2.2)$$

This Nyquist Frequency is the minimum sampling frequency for the correct recovery of a signal. That means the actual sampling rate  $f_{sampling}$  (sampling frequency) has to be at

least two times  $f_{signal,max}$  (maximum signal frequency).

Every increase of  $f_{sampling}$  above the  $f_{Nyquist}$  (Nyquist Frequency) is called oversampling.

To increase the performance of the DAC an OSR is introduced [12]:

$$OSR = \frac{f_{sampling}}{2f_{signal,max}}. \quad (2.3)$$

Tuning these two parameters, the resolution and the OSR, results in an increase of the SNR, as mentioned in 2.9 [12].

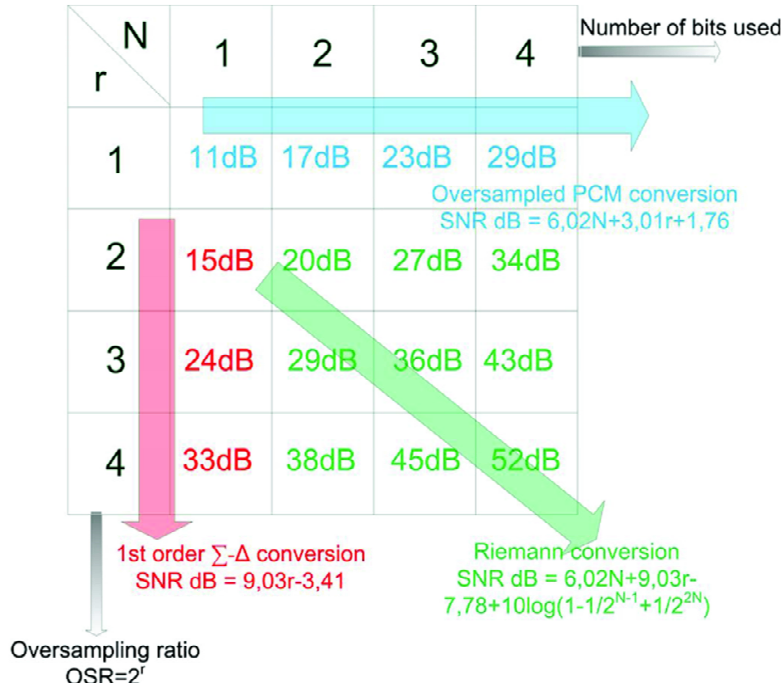


Fig. 2.9.: Table of theoretically SQNR (Signal-to-quantization-noise-ratio) over resolution and OSR [12]

The table states the theoretically achieved SNR with respect to these two parameters. The parameter N describes the number of bits used for the resolution and r the OSR, respectively. Here the OSR is defined as

$$OSR = \frac{f_{sampling}}{2f_{signal,max}} = 2^r, \quad (2.4)$$

which leads to

$$f_{sampling} = 2^{r+1} * f_{signal,max} \quad (2.5)$$

with respect to r. As you can see in Figure 2.9 the Riemann Conversion (green) performance is the best for a minimum number of bits and a OSR, with respect to the parameter r, of

two, respectively. Performing a digital-to-analog conversion with one bit resolution, the  $\Sigma - \Delta$  conversion fits the best. If no oversampling is considered, hence  $r = 1$ , a PCM (Pulse-code modulation) conversion is the best.

Every increase in the number of bits results will increase the SNR by 7 dB, while increasing the OSR, here the parameter  $r$ , will increase the SNR by 9 dB, for the Riemann Conversion. Equation 2.6

$$\text{SNR [dB]} = 6.02N + 9.03r - 7.78 + 10 \log_{10}\left(1 - \frac{1}{2}^{N-1} + \frac{1}{2}^{2N}\right) \quad (2.6)$$

describes the theoretically achievable SNR with the Riemann Conversion [12].

## 2.5. Conclusion of the fundamentals

In this chapter the implementation of the Riemann Pump in a system design has been presented. After the description of the classification and application, the concept of the custom DAC has been described. After explaining a simple charge pump, a multi bit resolution DAC have been presented. The designed custom DAC has been compared to conventional DAC concepts. A concise evaluation states that the Riemann Pump is a great improvement for conventional digital-to-analog conversion concepts.



### 3. Riemann Pump circuit design

The goal was to design an arbitrary waveform generator for a signal bandwidth of 6 GHz. For the implementation in a base station, the most promising technology was GaN (gallium nitride). GaN HEMTs (high electron mobility transistors) were used for the high speed switches, which served as a voltage controlled current source. Based on the chosen technology a suitable push-pull concept were found [13] to show the feasibility of the concept. The attention was rather drawn to proof the concept than to optimize for energy consumption or efficiency. In the design process a suitable load impedance and the right dimension of the used components had to be found.

#### 3.1. Approach and implementation of the Riemann Pump

As stated in chapter 2.3 the circuit needed high speed switches, which were capable to drive power. The absence of a p-type transistor in GaN technology made it challenging to find a suitable concept to realize the push-pull stage. Since the n-type HEMTs needed a negative gate source voltage  $V_{gs}$  (gate source voltage), the high side switch could not be implemented without a driver circuit. The source contact of the high side switch, realized by a n-type GaN HEMT, was connected to the output of the test circuit. Since the potential at the output was not constant, this high side switch needed a driver circuit. A suitable driver circuit was found in [13], where the principle of a push-pull stage for power applications is described. The benefit of the integrated driver circuit was the improved efficiency of switching. The transistor switching speed was determined by the dimension of the driver circuit. If the switching speed was increased, the gate driving current  $I_G$  (DC-component of the gate current) has to be increased to switch the transistors.

One possible approach to design a Riemann Pump is shown in Fig. 3.1.

On the left side, as marked, is the driver circuit which was needed to switch the high side transistor without dissipating a huge amount of power. As the timing is crucial for the switching process, the driver concept was implemented for the low side switch too. The schematic shows the first approach for realizing a Riemann Pump in GaN technology. The next step was the identification and calculation of a proper output capacitance, since it represent the input of a linear power amplifier where the desired signal is synthesized.

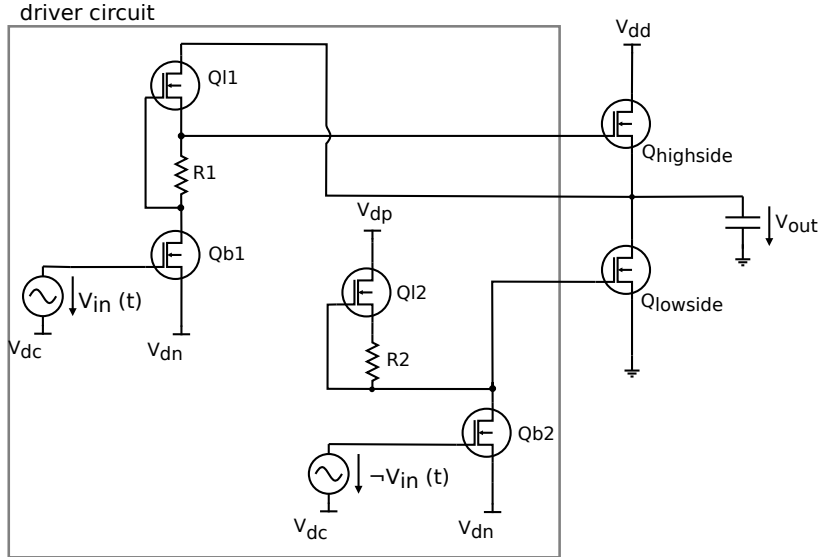


Fig. 3.1.: Schematic of a push-pull stage with corresponding driver circuit

### 3.2. Identification of the load impedance

The signal is generated at the input stage of a linear power amplifier, as described in 2. This input stage is modelled with a GaN HEMT with a gate length of  $0.25\text{ }\mu\text{m}$ . Considering a 20 W power amplifier for transmission purposes, led to a GaN HEMT with a total gate periphery of 4 mm, based on an approximation for the power density of  $5\frac{\text{W}}{\text{mm}}$  gate periphery [5], [14]. Simulations confirmed this approximation as an output power density of  $5.6\frac{\text{W}}{\text{mm}}$  at  $V_{DS} = 25\text{V}$  was measured. This transistor model HEMT (IAF\_GE\_MSL\_A204/IAF\_GaN25\_HEMT\_CS\_LS\_SHfull) used in ADS (Advanced Design System) were modelled at the IAF[15] and is based on a state-space approach. For simulation purposes four transistors were modelled in parallel, each with 8 finger and  $125\text{ }\mu\text{m}$  gate width to reach the required gate periphery. The simulated power amplifier is biased with respect to the maximum MAG (maximum available gain), which led to a bias of  $V_{GS} = -1.5\text{V}$  at  $V_{DS} = 25\text{V}$ . After the determination of the bias point, a S-parameter simulation yielded the input reactance of the power amplifier. Since the capacitive behaviour of the load impedance is of interest, the real part is for now neglected. The input reactance  $X_c$  is defined as:

$$X_c = -\frac{1}{\omega C}, \quad (3.1)$$

and is plotted in Figure 3.2 over the frequency range from DC to 6 GHz in a logarithmic scale.

As the reactance of the simulated power amplifier is nearly constant for the frequency of 1 GHz and beyond, this led to the assumption that frequency dispersion effects came into play. Interpreting the minus sign only for the phase delay, since it is capacitive, the absolute

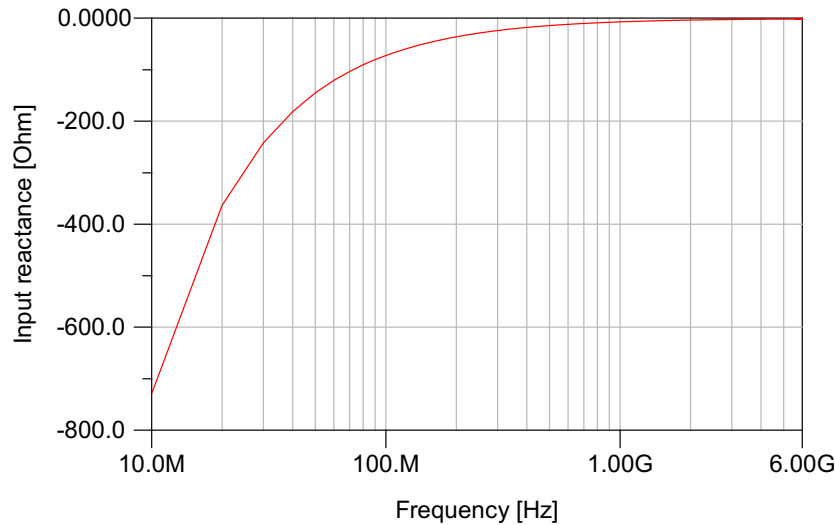


Fig. 3.2.: load reactance

value of the reactance decreases exponentially with the frequency up to approximately 1 GHz. Solving the equations 3.2 absolute value for the capacitance yielded:

$$C = \frac{1}{\omega X_c}, \quad (3.2)$$

which is illustrated in Figure 3.3. The frequency dispersion effect on the input capacitance of the GaN HEMT is seen in 3.3 for frequencies beyond 1 GHz.

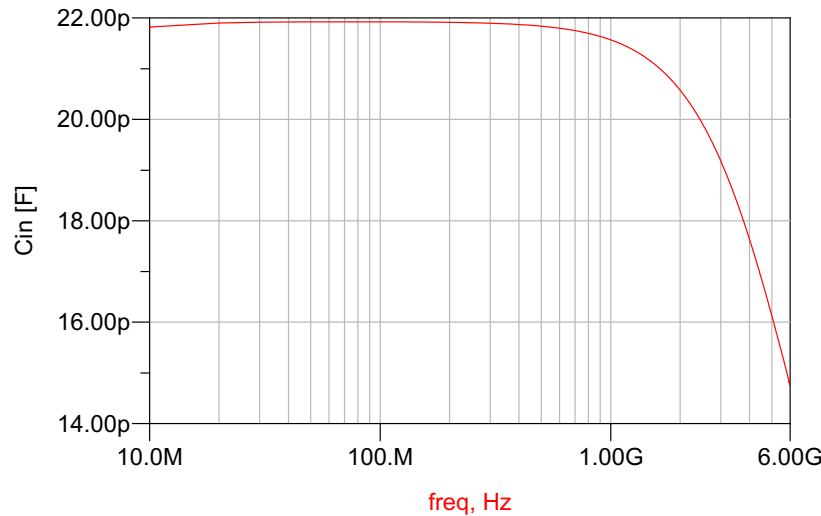


Fig. 3.3.: load capacitance log

Since the input capacitance can be assumed as

$$C = \epsilon_r \frac{A}{d}, \quad (3.3)$$

it follows that

$$C \propto \epsilon_r \quad (3.4)$$

and therefore for high frequencies, the capacitance is decreasing due to decreasing dielectric constant for GaN [14], p.7. Degrading capacitance due to non-linearities.

### 3.3. Dimension of the used components

An output capacitance of nearly 22 pF was found for the output linear power amplifier stage. Based on this calculation a proper test circuit was investigated. To avoid immediate clipping of the signal at the output, the transistor dimension had to fit. Since an oversized transistor would charge the capacitance and the signal would be clipped. Hence a transistor dimension was chosen which allowed to synthesize a decent signal. To synthesize a sine wave for the frequency of 6 GHz with a voltage swing of  $V_{swing} = 4V$ , the two greatest slopes were chosen. In the presented concept the resolution is three bit, hence eight different current slopes could be generated. The sequence of the relative slopes  $7i_0$  and  $5i_0$  synthesizes the rising edge of the sine wave. With this relative slopes and an oversampling ratio of four at the frequency of 6 GHz, led to a sampling time  $\Delta t$  of 20.83 ps, since the sampling frequency is eight times the signal bandwidth.

The current-voltage relation for the capacitor

$$I = C \frac{dU}{dt}, \quad (3.5)$$

is used to determine the reference current  $i_0$ .

A voltage swing of  $V_{swing} = 4V$  is equal to an amplitude of  $\hat{v} = 2V$ . The oversampling of four yielded, that the sine signal is sampled by eight points. Hence the rising edge consisted of two sampling points. The first sampling point with the relative slope of 7 and the second of 5, respectively. Integrating the current for two different samples yield:

$$\int_{\Delta t} 7i_0 d\tau + \int_{\Delta t} 5i_0 d\tau = C * U, \quad (3.6)$$

and solving for  $i_0$  resulted in:

$$i_0 = \frac{U * C}{12 * \Delta t}. \quad (3.7)$$

For the assumption to reach nearly a voltage of  $\hat{v} = 2V$  for two sampling intervals ( $2\Delta t$ ) and the capacitance of  $20 \text{ pF}$  it resulted a reference current of  $i_0 = 160 \text{ mA}$ . As simulations showed, a reference current of  $151 \text{ mA}$  could be established with a dimension of the voltage controlled current source, high side switch, of  $UGW = 100 \mu\text{m}$  and gate finger number of eight. Hence the gate periphery for the reference current source is  $800 \mu\text{m}$ . To ensure proper switching the driver circuit dimension had to be optimized. Since the driver circuit worked as a current source, the dimension of the transistors and resistors were tuned to achieve a proper current to switch the power transistors fast and efficient. The dimension of the driver transistors were approximately a quarter of the power transistors, the switching high and low side transistor. The resistor values were achieved by tuning with respect to power consumption. Further details on the driver circuit and its properties, see [13]. The schematic is designed with ADS, see Appendix A. As the dimension of the power stage scales with the factor of two so the driver circuit dimension do.

### 3.4. Circuit design summary

As no complementary transistors were available in III-V technology a proper driver circuit had to be investigated. Further the speed of the switches was crucial as a broadband signal should be synthesized, which led to the implementation of a known concept [13] for the driver circuit. A low loss, high speed, digital controlled driver circuit was implemented. Using this concept had the advantage of verification and validation. It was difficult to determine the reference current since the switching is not ideal, a leakage current through the driver circuit occurs and the current had to be probed in the transient state. The problem of not perfect switching is, that the channel is opened and closed slowly in comparison to an ideal switch. This increase the current with the increase of charges flowing to the transistors gate. Therefore the reference current is time-averaged. The circuit design and simulation combines the dc state with the rf state. For a dc simulation the current through a capacitor is zero. Further the loaded voltage controlled current source was not defined for the given output load. The dimension of the used components determined the resulting voltage step. A typical (draw-back) contradiction was a small transistor dimension could synthesize signals to a very low signal frequency while a bigger one would fully charge the output capacitor which will clip the output signal, for a given oversampling ratio. Because then the sampling time is fixed. If the transistor dimension is chosen to be bigger, the higher signal frequency could be synthesized with a decent voltage swing but the low signal frequencies would turn into a rectangular shape. This problem restricted the signal bandwidth to be smaller than from DC to 6 GHz.



## **4. Circuit simulations for generating various waveform signals**

The circuit simulations were run to validate the behaviour of the conceptual design. Some fundamental ideas to understand the trade-offs of the designed circuit were identified with these simulations.

A harmonic balance simulation was used to investigate the concepts of chapter 3. The benefit of the harmonic balance simulation, done with the tool ADS, was that the whole system was modelled in a steady state mode, so that no transients influenced the results. This aspect was important due to the non linearity of the circuit. In a first step the generation of an analog output signal was checked. The analog signal in the time domain was plotted to check the feasibility to synthesize a signal. After various signals were synthesized, a short stability and energy consumption analysis was performed.

The stability check was needed to validate that the circuit did not oscillate. As well the circuits energy consumption had to be checked, since it could be implemented in mobile devices. In the last step a simulation was run which made the concept comparable to the realized circuit. In this simulation the transistor dimensions were adapted to the dimension of the built demonstrator. This should give an insight to the behaviour of the constructed demonstrator.

The detailed modelling and simulation of the designed circuit under real conditions, considering all loss effects would go beyond the scope of this thesis. Therefore a keep it small and simple approach was chosen.

### **4.1. Generating various analog signals with digital input control**

The generation of analog signals at the output of the designed circuit was the purpose of this concept. The designed Riemann Pump should be able to create various waveform signals by converting a digital bit sequence into the analog output signal. Simulations in time domain were required to validate the signal integrity of the synthesized signals. Plots in time domain represented the output signal of the circuit. The signal was generated by

integrating a current over time which charged a capacitor. To synthesize a certain analog signal at the output, the corresponding Riemann Code was needed. Due to the fact that no algorithm existed which could compute the Riemann Code, it was done manually.

The presented DAC had a resolution of three bit and synthesized signals with an OSR of four. The components used, were optimized with respect to the signal integrity. The dimension of the used components were tuned while simulation to get the desired output signal. In contrast to this optimized components, chapter 4.4 deals with the simulation done with real dimensions of the demonstrator components.

#### 4.1.1. Sine wave generation in the time domain

As known from basic signal processing the sine wave for continuous time is the elementary signal and therefore synthesized first. For the generation of this sine wave a corresponding Riemann Code was required which will be converted to the analog output signal.

This Riemann Code was generated by hand via an approximation of a sine wave with a sequence of eight different slopes. Eight different slopes represented a three bit resolution of the DAC. In order to achieve a OSR of four the sequence consisted of eight sampling points.

Figure 4.1 presents the sequence of slopes used to approximate a sine wave.

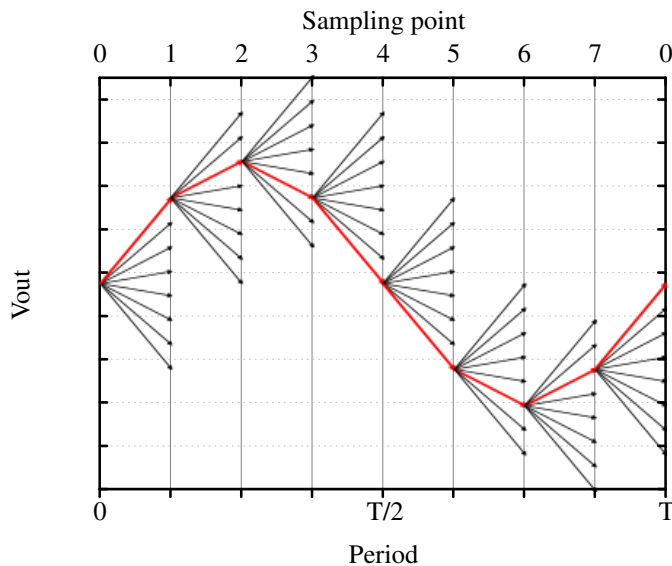


Fig. 4.1.: One possible approximation of sine wave generation to get the Riemann Code

This sequence of slopes, referred to  $i_0$  values, is:

$$+7 \quad +3 \quad -3 \quad -7 \quad -7 \quad -3 \quad +3 \quad +7, \quad (4.1)$$

which represents the following Riemann code:

$$000 \quad 010 \quad 101 \quad 111 \quad 111 \quad 101 \quad 010 \quad 000. \quad (4.2)$$

The Riemann Code consisted of eight triplets where each triplet represents the three different switches. The number of triplets represented the number of sampling points corresponding to the OSR. This particular generated Riemann Code was used to synthesize sine waves in the frequency range between 500 MHz and 6 GHz, as shown in Figure 4.2.

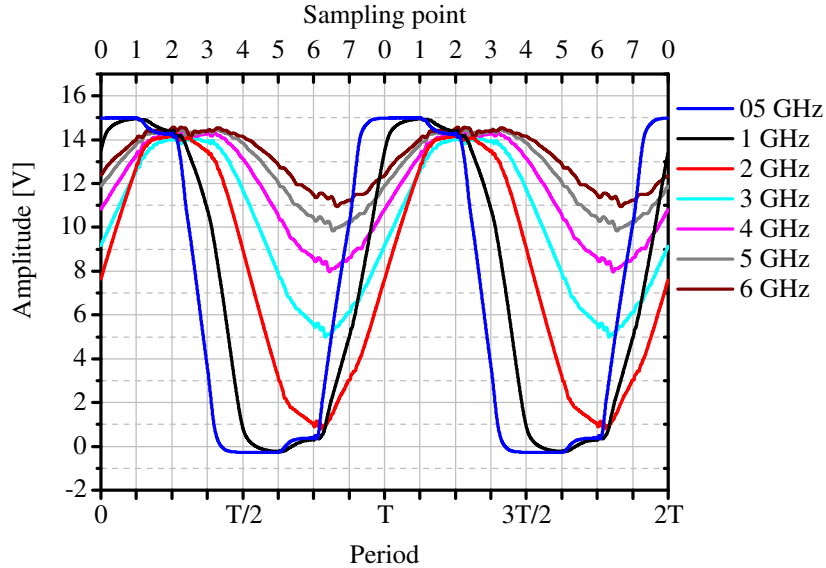


Fig. 4.2.: Synthesized signals with demonstrated Riemann Code for the frequency range of 0.5 GHz to 6 GHz

Seven synthesized signals generated with the same input but with different sampling frequencies are demonstrated in Figure 4.2. Here the signals amplitude was plotted over two periods in time domain.

Due to the different absolute sampling times, the amplitudes of the signals differed. The maximum reachable amplitude was the supply voltage, here set to 15 V.

Once the amplitude reached the supply voltage, the signal wave form is clipped and transforms the sine wave into an rectangular form. The shape from most of the plotted functions fit fairly to a theoretical sine wave. But Figure 4.2 also highlights already some limitations of the designed circuit, as the blue curve turns into a rectangular signal form.

The circuit designed in chapter 3 was tuned to cover the frequency range from 1 GHz to 6 GHz fairly well, if a voltage swing of two volts would be still acceptable. Below the frequency of 1 GHz the desired shape of a sine wave was going to be rectangular due to the long sampling time as demonstrated in Figure 4.3.

The blue signal which should represent a sine wave with a signal frequency of 500 MHz was clipped and showed the behaviour of a rectangular signal. A fully charged capacitor induced this undesired behaviour. In addition to the rectangular signal wave form another

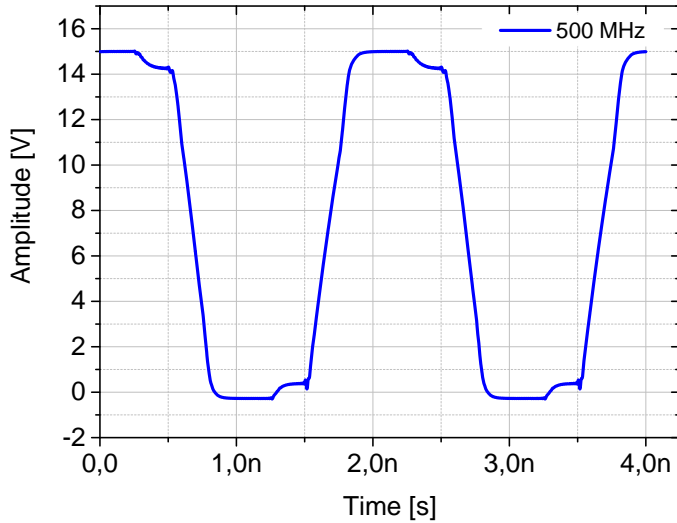


Fig. 4.3.: Synthesized sine wave for frequency of 0.5GHz

distortion is visible. At the sampling time when the fully charged capacitor is discharged and when the fully discharged capacitor is charged, a distortion is shown which is induced by a leak current. This leak current is induced by the commutation time, which induced a leak current over the driver network. (→ **insert figure?**)

The signal frequency of 1 GHz represented a lower bound on the frequency range in the configuration referred to chapter 3 of the circuit. No sine wave could be synthesized below this limit. The upper bound of the frequency range is limited to the detectable voltage swing. If a voltage swing of 2 V would be still accepted, the upper bound would be a signal frequency of 6 GHz.

Figure 4.4 compared a theoretical sine wave signal (red) with a synthesized one (black) for a frequency of 1 GHz. The synthesized signal was the same black curve as in Figure 4.2. In general the sine wave is of the form:

$$v(t) = V_{DC} + \hat{v} \cdot \sin(2\pi f \cdot t + \phi). \quad (4.3)$$

The synthesized signal (black) in Figure 4.4 fit pretty good to the theoretical sine wave, which had an amplitude of  $\hat{v} = 7.5$  V, a signal frequency of  $f = 1$  GHz, a phase shift of approximately  $\phi = \pi/4$  and an DC offset of  $V_{DC} = 7.5$  V.

Although it seemed to be a good fit, two distortions were visible in the peak and the valley of the synthesized signal. **As mentioned earlier for figure 4.3 this is a leakage current induced by the commutation.** Since the digital to analog conversion always introduces noise to the signal, refer to chapter 2, the fit was not perfect.

Figure 4.5 highlighted the difference between the synthesized and the theoretical sine wave form in a more detailed way.

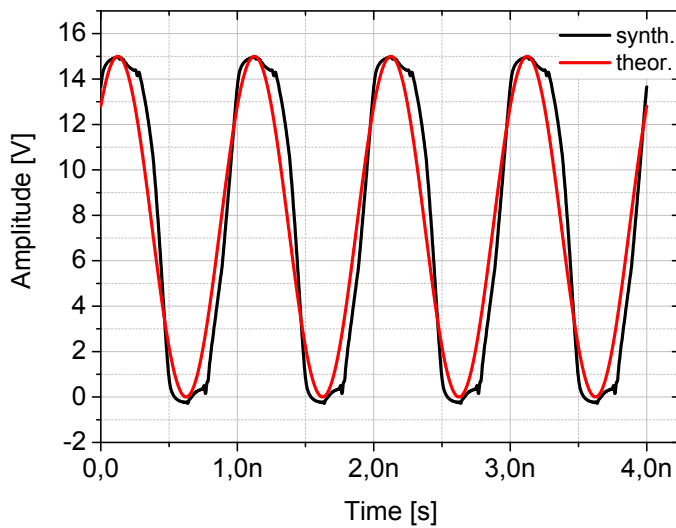


Fig. 4.4.: Synthesized sine wave with the theoretical sine wave

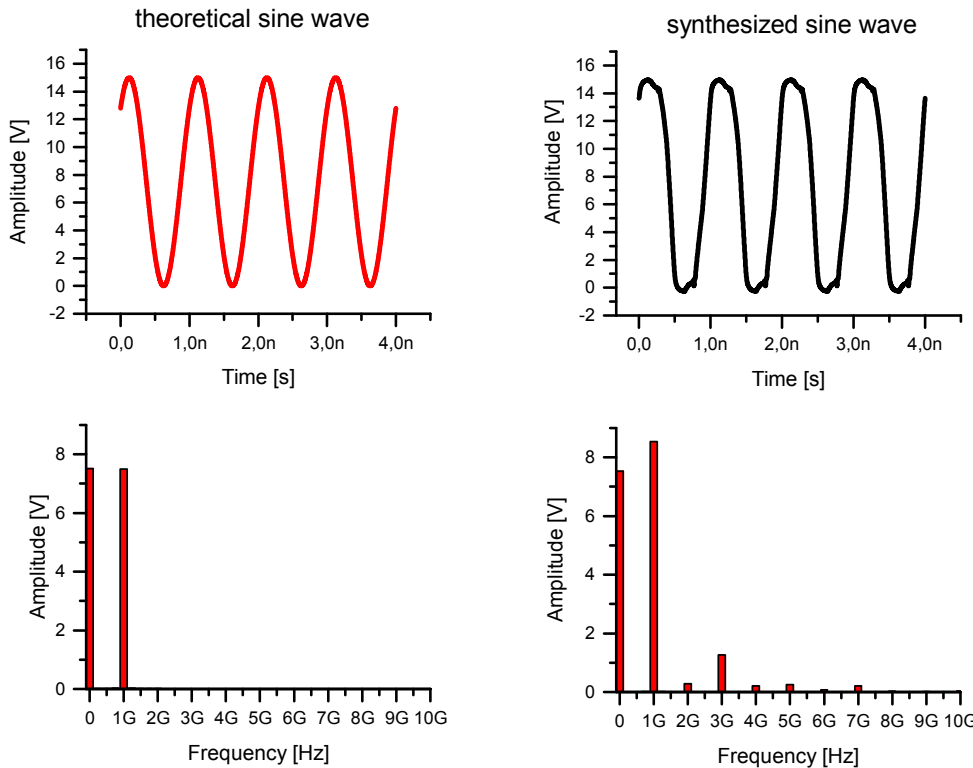


Fig. 4.5.: Comparison between a theoretical and a synthesized sine wave with their spectrum

A theoretical sine wave is compared to the synthesized one with their corresponding spectra. The spectra of signals were a lot easier to compare, in contrast to the time domain signal, with respect to the accuracy. Since the spectrum of a perfect sine wave only consists of a DC part and the harmonic frequency it was easy to check whether the generated signal fit.

On the top left side of Figure 4.5 the theoretical sine wave is plotted in time domain. Underneath of it the spectrum presented a frequency portion for the direct component at 0 Hz and a fundamental frequency portion at 1 GHz. This Fourier transformation represented the frequency portions of a clear sine wave.

The synthesized sine wave on the top right side fit fairly well to the theoretical one. The spectrum of the synthesized signal showed nearly the same behaviour as for the theoretical one. Beside the direct component and the fundamental frequency component there were some additional unwanted frequency portions which distorted the signal. The maximum distortion was about 1 V in amplitude at the third harmonic. The 2nd to 10th harmonic were at most half of a volt in absolute value of the amplitude. **The calculated SNR was 15.2 dB. The ideal SQNR of the Riemann conversion in this configuration is 27 dB.**

As the sampling frequency could be changed to tune the signal frequency of the output signal it was also possible to change the input control sequence to manipulate the shape of the signal. Due to the three bit resolution there was a limited number of different slope combinations to synthesize a sine wave. In fact the limit was bound to six different combinations for synthesizing the sine wave, namely: 75, 73, 71, 53, 51, 31 with respect to the  $i_0$  values. The first digit indicated the slope of the first sampling point and the second digit of the second sampling point of a rising edge from a sine wave, respectively. The falling edge of the sine wave consisted of the negative values of the mentioned slopes.

The six different combinations were plotted in Figure 4.6 over two periods for the signal frequency of 3 GHz.

Figure 4.6 presented the different shapes of a synthesized sine wave for a frequency of 3 GHz. This was utilized to calculate the Riemann Code which fit best to the theoretical signal.

#### **4.1.2. Rectified sine wave generation in the time domain**

Beside the generation of the full sine wave, a rectified sine wave was simulated as well. Based on the same approximation principle as demonstrated in figure 4.1, the corresponding Riemann Code for the rectified sine was generated, namely:

$$000 \ 001 \ 010 \ 011 \ 100 \ 101 \ 110 \ 111. \quad (4.4)$$

As the rectified sine wave consisted only of the positive wave form over the full period, the oversampling ratio is performed on half of a sine wave. This resulted in a more precise wave form, since the rising and falling edges could be synthesized in more detail. For

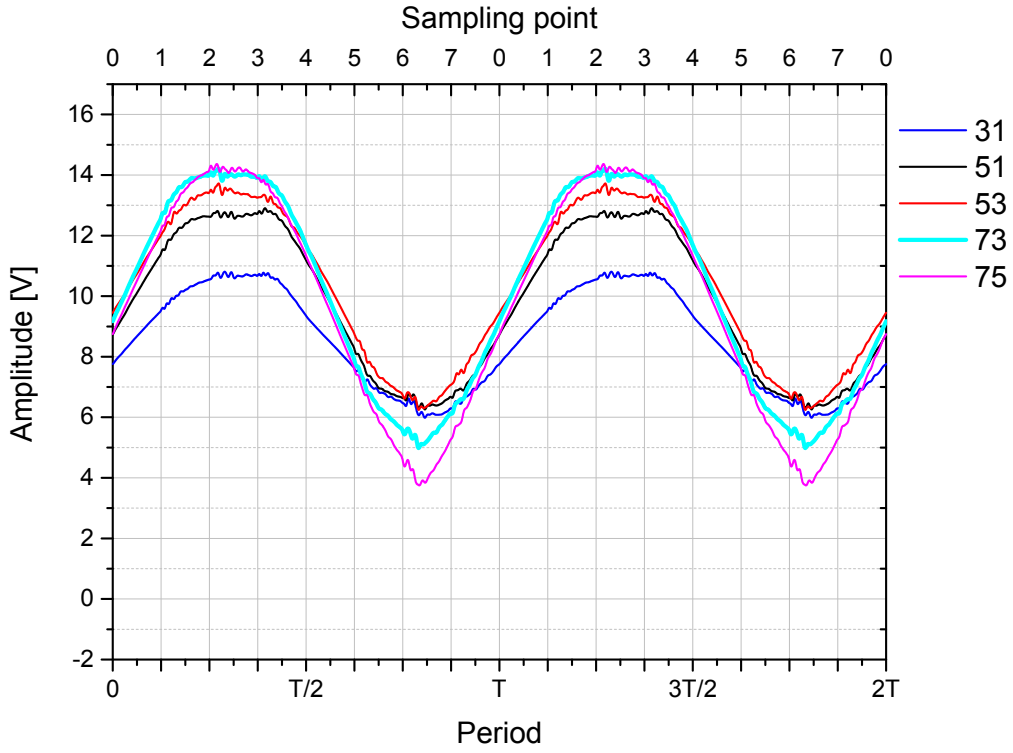


Fig. 4.6.: Signals with the same signal bandwidth 3 GHz but different input control

the sine wave the rising edge resulted in two different slopes, which was doubled for the rectified sine wave. Hence the rectified sine wave consisted of eight sampling points, while the corresponding positive half of a sine wave only consisted of four sampling points. The rectified sine wave exhibited the sequence of all eight different slopes, from the biggest positive to the biggest negative slope.

A few signals with different frequencies were simulated and plotted in figure 4.7, which used this Riemann Code.

As expected the rectified sine wave fit very good to the theoretical. The rectified sine wave was synthesized in more detail, since the oversampling ratio were doubled effectively. The oversampling ratio of four for the full sine wave correlated to eight sampling points for the whole period. Since the sine wave consisted of a positive and a negative part, only four sampling points were used for the positive wave. As the rectified sine only consisted of one positive part, eight sampling points could be used to synthesize this positive wave. Therefore this result reflected the behaviour for a sine wave if the oversampling ratio would be doubled. Too big absolute sampling times drove the signal into clipping for the generation of a rectified sine wave. This effect was seen in Figure 4.7 for the blue curve which had a fundamental frequency of 500 MHz. Since the absolute maximum voltage which could be reached was the supply voltage. The shapes of the signals with

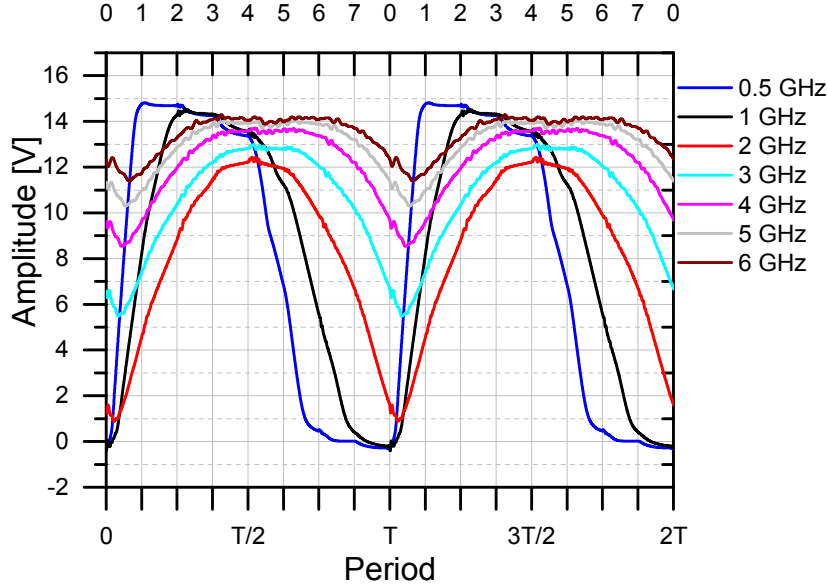


Fig. 4.7.: Signals with same slope but different signal bandwidth

fundamental frequencies 2 GHz to 6 GHz fit very good to a rectified sine, as seen in Figure 4.7. The same issues, drawbacks and limits were presented here as for the full sine wave. All simulations done to synthesize various signals confirmed the proof of concept.

#### 4.1.3. Triangular wave generation in the time domain

Beside the most common signals another signal was synthesized. A triangular signal was chosen to validate the feasibility of generating arbitrary waveforms. The wave form of a triangular signal represented the push-pull stage charging and discharging a capacitor similarly. As the time for charging and discharging was the same, a good fit was achieved. All simulations so far were run with a three bit resolution of the realised circuit. These three bit resolution represented eight different slopes, and therefore for a similarly charge and discharge process four different slopes could be used. These four slopes were +7, +5, +3, +1 for the charging process and their counterparts -7, -5, -3, -1 for the discharging. Hence the sequences of slopes were named: 11, 33, 55 and 77, with respect to  $i_0$  values. Figure 4.8 demonstrated the four different combinations for synthesizing the triangular wave form.

The signals were distinguished by the set of slopes used for synthesizing this shape. The fundamental frequency was set to 2 GHz, representative for the frequency range of 500 MHz to 6 GHz. Only the wave form for the biggest slope 77 seemed to shape like a rectified sine while the other three signals seemed to fit to a triangular wave very nicely. This effect was caused, as mentioned earlier, by the sampling time and the high current



Fig. 4.8.: Triangular signal with same signal bandwidth but different slopes

values. This led to a clipping effect at the maximum voltage.

Representative for the four combinations to synthesize this triangular signal wave form, figure 4.9 demonstrated for the slope of 33, the frequency varying signals from 500 MHz to 6 GHz.



Fig. 4.9.: Triangular signal with same slope but different signal bandwidth 3GHz

## 4.2. Stability analysis of the realised circuit

To guarantee the proper function of the circuit a short stability analysis was performed. This analysis was necessary to check if the circuit oscillates. To prevent the circuit to take damage this oscillation had to be avoided. This analysis was important to ensure that the DUT (device under test) was stable for the whole frequency range used. Then the complex impedance was calculated and checked if it could start an oscillation.

To check the stability the real part of the impedance had to be positive. A basic definition of passive elements were that they have a reflection coefficient magnitude less than unity. Checking the input reflection coefficient, the values had to be inside the unity circle. Therefore no negative resistance would be allowed to occur since that can lead to unwanted amplification and oscillation which can damage the circuit. Because the real part of the impedance at all measurement points were positive for the whole frequency range, the circuit seemed to be stable. The stability check was performed within the ADS tool.

## 4.3. Energy consumption analysis of the realised circuit

As the concept was designed for the use in mobile communication, it could be implemented in mobile devices. Since the energy storage of mobile devices is limited, it is important to get a decent power dissipation for the whole circuit.

$$P_{cond} = R_{DS,on} dI_0^2 \propto R_{DS,on}$$
$$P_{sw} = \frac{1}{2} V_{in} I_0 (t_{on} + t_{off}) f_{sw} \propto f_{sw}$$

In addition to the stability analysis the energy consumption analysis was important with respect to the use in mobile devices. The losses in the circuit were those static losses while the switches plus driver is in one state. The dynamic losses were those which occur during the switching... Definition, expectations, simulations...

There were the trade off between the power consumption of the high side switching transistor and the switching behaviour. Since the switching process needs to be very fast a high current is needed. This are losses. The driver circuit has to be optimized to reduce the energy consumption while maintaining the the switching process correctly. If the correct hard

For the chips used for the demonstrator refer to the work of Stephan Maroldt who states, that the power consumption is divided into static and dynamic ones. The switching losses are greater than the static ones. In fact of the high energy consumption, the realized DAC is designed for the integration in a base station.

## **4.4. Proof of concept simulation with existing components**

Schematic of the measurement setup, esb. Simulation regarding the measurement, +3 and +1 triangular waveform. frequency 100mhz and 150mhz, vdd = 5, vdp=0V, vdn=-5V. As DDRi2C is used, bottom vdp(in na; lowside) = vdd. Sim RP\_DDRI\_XY6\_v1\_sim To combine the measurement results with the presented theory, some simulations were done with the dimensions of the real demonstrator. It provided a basis of what can be expected. Therefore the simulation was adapted to a two bit resolution with much greater power transistors. To compare the results simulated here and measured in chapter 6 the switching frequencies was kept at lower frequencies (100 MHz).

## **4.5. Evaluation of the simulation results for the Riemann Pump**

1. different wave forms can be synthesized
2. the signal bandwidth is restricted to a smaller one than desired
3. parasitic effects and losses degrade the signals waveform
4. the system is stable
5. the energy consumption is in the range for base stations
6. dut is not optimal w.r.t. efficiency

The simulation results confirmed the feasibility of the chosen approach. Some trade-offs in mind and the ability to change some system parameter made it possible to generate some good fitted signal waveforms.



## 5. Realisation of a demonstrator

The demonstrators realized in this work consisted of several MMIC (microwave monolithic integrated circuit) chips with a filter network built by discrete elements. Due to the fact that SMD (surface mounted device) decoupling capacitors as well as MMIC were used, this were called hybrid test circuit. For assembling and measurement purposes the test circuit was restricted to a resolution of two bit. Otherwise the bonding, assembling and controlling of the inputs would became too complex. Two bit resolution implied to create an input control strategy for the four inputs. A third bit of resolution would enhance the performance but also increase the complexity of the realisation as six inputs needed to be controlled.

A two layer high frequency substrate, namely Rogers RO4003, were used. The benefit of the low dissipation factor, a low tolerance of dielectric coefficient and the stable electrical properties made this the most suitable material for the broadband application.

With the help of former designed chips, two different versions of the substrate were designed. To make use of these chips it was necessary to design two different versions due to the different properties of the chips. The two layer substrates were ordered with a thickness of 0.508 mm, a 35 µm Cu conduction layer and a ChemNiPdAu metallisation. An impedance control ensured the correct impedance of  $50\Omega$  for the 1.1 mm wide MSL (microstrip line) at the in- and output of the circuit.

Each version of the designed substrates had the size of 60 mm x 54 mm while the area for the multi assembled chips covered approximately 6 mm x 5.5 mm for both. One layout was designed for chips which ground contact were plated through the backside metallization of the chip. Yielding a power transistors source contact connected to these ground plates. This property yielded a great drawback compared to the other layout.

The second layout of the substrate were planned to improve the heat transfer by using another type of chip. This chips ground contact were not plated through the backside metallization, making them suitable for soldering on a conducting heat spreader.

To make use of the former designed chips, these two layouts were designed to enable the proof of concept.

## 5.1. Substrate layout using DDRi\_X6 and DDRi\_Y6 chips

The presented layout of the substrate was designed for the use of the chips DDRi\_X6 and DDRi\_Y6 since the chip DDRi\_2C required a different multi chip connection. Figure 5.1 shows the overview of the designed substrate, consisting of a decoupling capacitor network, several dc voltage and RF connectors and the core of the circuit.

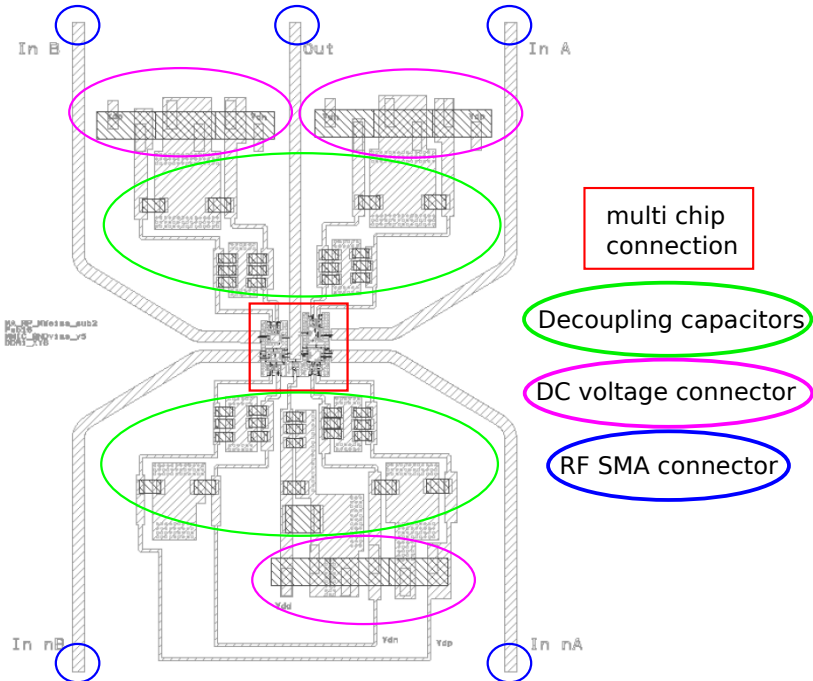


Fig. 5.1.: Layout substrate with DDRi\_XY6 chips

It is to mention that the layout outside the red marked box was very similar for the others version. So one explanation of the layout outside the box were sufficient. Only one additional DC voltage supply line was added and the arrangement of the chips were different. Due to the different arrangement of the chips attention was paid to the connection of bias voltages.

The described part outside the red box consists of the SMD decoupling capacitor filter network and the multi pin connector for the DC voltage supply. In addition to this the in- and output transmission lines were designed to fit to an  $50\Omega$  impedance.

The decoupling capacitors, also known as bypass capacitors, filtered out undesired frequency portions by the power supply. If the filter network did not work properly, this could lead to undesired oscillations of the circuit. Following a very common design rule lead to the right choice of capacitors. A very first decoupling capacitor was integrated on the MMIC chip. The requirement to place the decoupling capacitors as close as possible to the DC voltage supply pad lead to the choice of a special MMIC capacitor. It was

possible to place that capacitor as near as possible to the chip to keep the length of the bonds small. To avoid resonance peaking the most suitable capacitors were those with a high ESR (equivalent series resistance) since the quality factor of these were small. A great bypassing range were enabled by choosing a 82 pF capacitor, namely D20BT820K5PX from Dielectric Laboratories Inc., to filter out frequencies in the GHz range. The gold metallization (for wire bonding), the thin film technology and the custom sizes (to keep it small), made this the most suitable capacitor for the purpose filtering high frequencies. Each capacity, of subsequent capacitors, were increased by one order in magnitude yielding the biggest capacity of 10  $\mu$ F. The big capacity filtered out frequency portions in the lower kHz range. In addition to the capacity also the temperature and voltage range had to fit. The following choice for the capacities was taken: 82 pF, 1 nF, 10 nF, 100 nF, 1  $\mu$ F, 10  $\mu$ F, started at the chips supply pin.

In fact that oscillation still could appear, the size of the used pads was designed larger, making it possible to change (adapt) the capacities for the filter network. These pads also had some via holes to transfer the ambient temperature to the backside. This was the attempt to keep as much as possible heat away from the chips.

The four input lines, as well as the output line, were designed to fit to an impedance of  $50\ \Omega$ . With a line calculator, namely line calc in the program ads, the corresponding line width was calculated. The calculated width of the line was 1.1 mm which was checked by the manufacturer with an impedance control as well.

The arrangement of the chips was realised to keep the length of the bond wires as short as possible. However the distances between conduction lines were limited by the process of the manufacturer. The transmission lines of the signal path were designed to fit each other. All transmission lines were matched to  $50\ \Omega$  and got the same length to avoid undesired delays of the signal. An important fact to consider was that all switches had to switch synchronous at the same time. Therefore no signal delays were permitted, induced by different transmission lines.

The assembly of the multi chip connection marked with the red rectangular is described in Figure 5.2.

The drawback of these chosen chips were its plated through ground contact. In fact of this, a proper function of these chips as a high side switch, made it necessary to place it on an electrical isolated pad. At the bottom of Figure 5.2 these chips were placed on an isolated pad. This pad did not have any connection to the backside potential of the substrate. The pads were surrounded by a large conducting layer with via holes to spread the heat. The idea was to dissipate the heat over the air bridge, through the via holes of the conducting layer, to the backside of the substrate. The substrate was mounted on a beam(?), which improved the cooling a little bit. The beam was necessary to install the

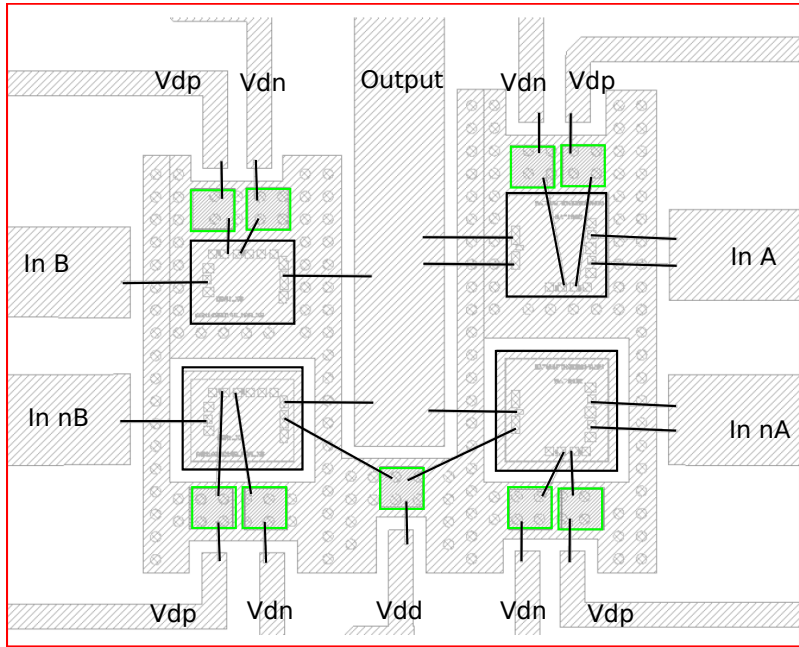


Fig. 5.2.: Layout DDRi\_X6 and DDRi\_Y6 chips

RF-SMA connectors and therefore the connection between the circuit and the measurement equipment. This was a very critical design issue since the chips created much power, hence much heat.

As mentioned earlier the length of the bond wires were set to be equal for the signal paths. Since an in-phase control of the input was important to ensure the switches to turn on/off synchronous. The length of the bond wires providing the DC voltage supply were not critical. The diameter of the wedged Au (aurum; Gold) bond wires was set to  $25\text{ }\mu\text{m}$  which ensured a maximum current of approximated 1 A for a bond length of 1 mm. The small diameter and the short length made it most suitable for the high frequency application.

Figure 5.3 shows the assembling of the used chips with their corresponding bond wires. As mentioned the bond wires got the same length for the signal path.

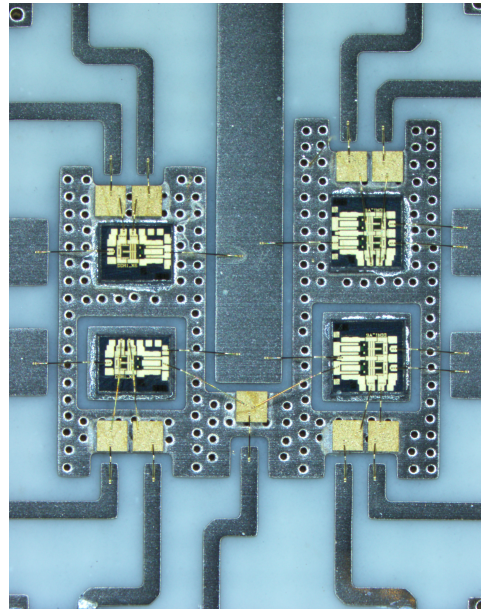


Fig. 5.3.: Photograph of assembled DDRi\_X6 & DDRi\_Y6 chips

## 5.2. Substrate layout using DDRi\_2C chips

The layout of the filter network and the DC supply voltage did not differ as much from the previous presented layout version. In this second layout one additional DC connector was added and the arrangement of the chips differed. Figure 5.4 shows the arrangement of the used chips, namely DDRi\_2C.

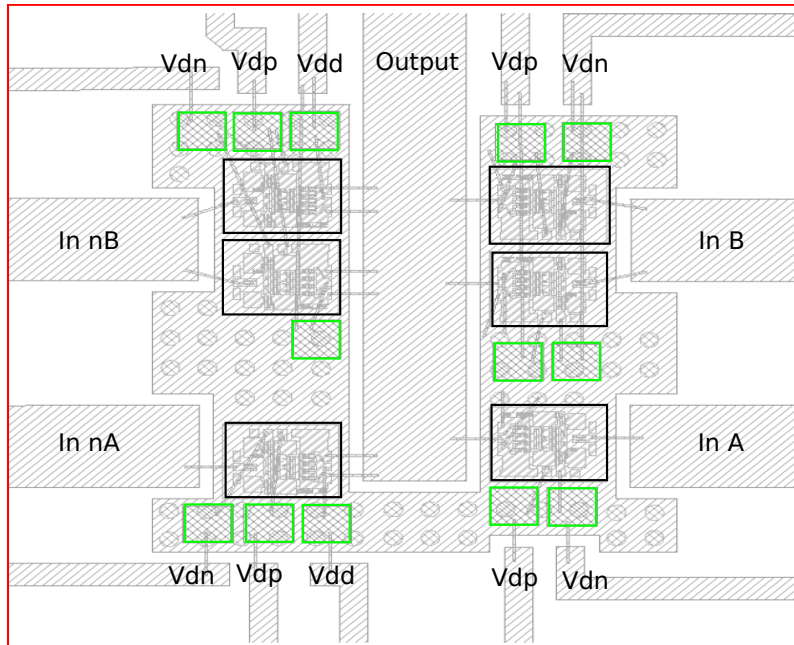


Fig. 5.4.: Layout DDRi\_2C chips

Due to the fact that six chips were used in this layout, the wiring of bonds was more

complex. Also the placement of the high and low side switches differed in contrast to the previous layout. The switches, representing one bit of resolution, were placed horizontally while the previous layout showed the switches placed vertically. Horizontal alignment was chosen due to easier bond wiring. This led to a different bias voltage connections.

The most important difference in the two layouts were the difference of used chips. The chips used in this layout version, DDRi\_2C chips did not have a plated through hole to its backside. Thus, these chips could be soldered directly to the heat spreading backside connected layer. The heat could transfer directly from the backside of the chip through the via holes to the substrates backside. This improved the heat transfer a lot in contrast to the first design. It must be pointed out to connect the ground potential of the chips separately to the boards ground potential. This version might work better due to the better heat dissipation, although the fabrication of the chips was older (2011).

The assembled chips for the second version is shown in Figure 5.5.

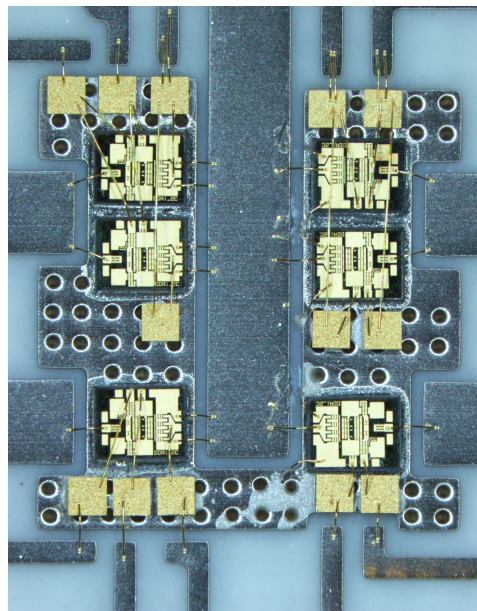


Fig. 5.5.: Photograph of assembled DDRi\_2C chips

### 5.3. Evaluation of the design and realisation process

In the realisation and layout process many things had to be considered.

The circuit was built on a hybrid assembly which combines the MMIC with the discrete SMD components on a Rogers 4003 substrate.

The input and output lines on the substrate were MSL which were matched to  $50\Omega$ . Important for the design of the input lines were that they are of the same length, due to timing issues. The input timing is crucial due to the fact that the switches have to switch synchronous. The output line was matched to  $50\Omega$  to ensure proper measuring.

In addition to the same length of the input lines, also the bond wires of the in- and output to the MMIC chips had to be of the same length. One of the most important and crucial things was the dissipation of heat. Based on the designed chips, two different concepts were chosen to dissipate the heat in the most proper way.

The wafer run of the chips DDRi\_2C was from the year 2011 and therefore five years old and hence the taping of the wafer could be not as good as the newer ones.

For bonding  $25\mu\text{m}$  (diameter) Au bonds were used. The length of the bonds were given by assembly limits for spacing of conducting layers due to manufacturer process limits.

In- and output connectors were commercially available SMA jack connectors with a matched impedance of  $50\Omega$  to connect standard RF cables.

The two layouts were fabricated by CONTAG AG while the needed components were ordered at Digi-Key Electronics.

The finished demonstrator is shown in Figure 5.6 with a short description of the placed elements.

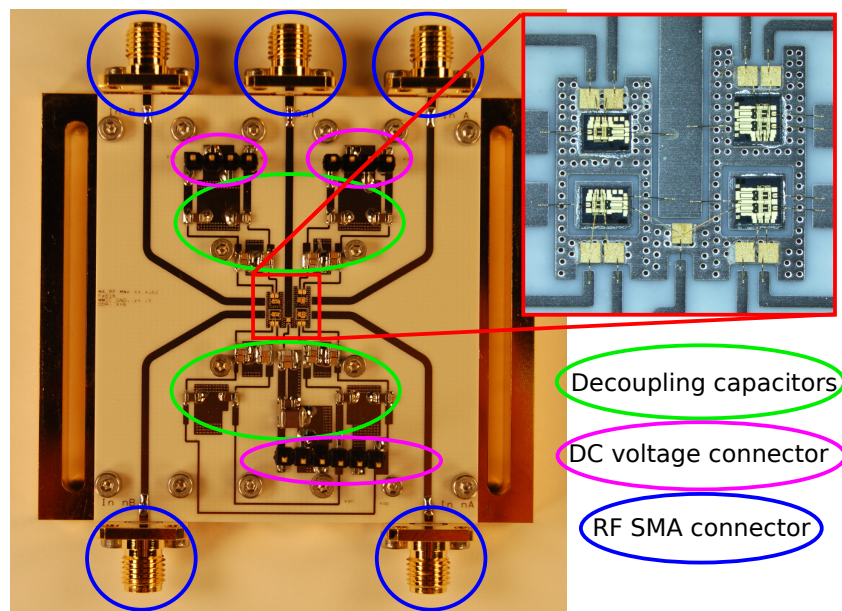


Fig. 5.6.: Assembled demonstrator

An improvement for the layout, could be to solder the DDRi\_XY6 chips on an electrical insulator while thermal good conductor, as AluminiumNitrid (AlN: 180-200 W/mK -> datasheet). This is needed to ensure the isolation from the output port to ground potential, but still have a good thermal transfer. This approach would have required only a small amount of the material AlN, which had to be cut very precisely into very tiny pieces, since the size of the chips DDRi\_X6 and DDRi\_Y6 were 1.25 mm x 1 mm and 1.25 mm x 1.25 mm, respectively. This pads adhered or soldered to the conduction layer ensure a good heat transfer.

In fact of the very small and precise size of the special material this was too costly for a first prototype to proof the concept.

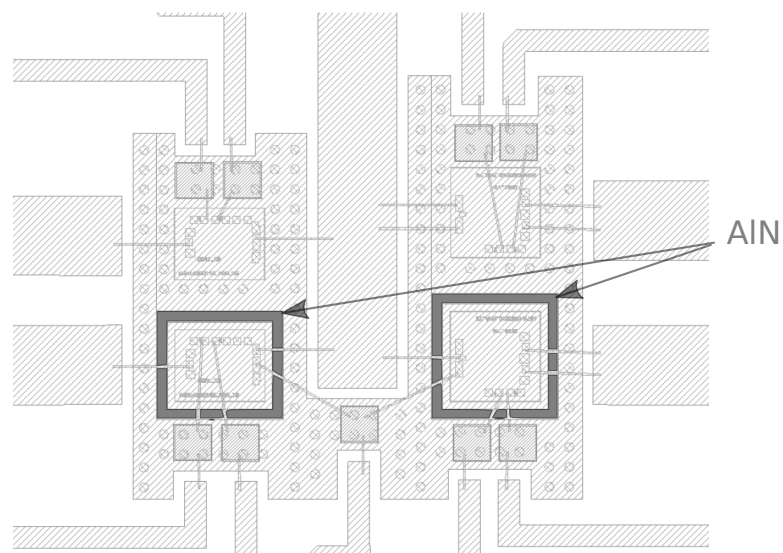


Fig. 5.7.: Improved layout for Chips DDRi\_X6 and DDRi\_Y6

# 6. Measurement of the realized circuit in the time domain

The aim of the measurement was to show the generation of different signals.

With respect to produce a decent signal waveform at the output, the assembled hybrid test circuit was terminated with a  $50\ \Omega$  termination and a  $3.3\text{ nF}$  capacitance, respectively. In contrast to the calculated capacitance of  $20\text{ pF}$  in chapter 3, a over dimensioned capacitor of  $3.3\text{ nF}$  terminated the output to ensure that the signal would not be clipped.

After the calibration of the measurement instruments a stability check was performed to ensure that the test circuit do not oscillate. In a next step the output of the circuit was measured with a resistive load to show the function of the push-pull stage. The correct functioning of the push-pull stage enabled the measurement with a capacitive load to synthesize a triangular waveform. In order to avoid any kind of damage the measurement was performed with low DC supply voltages.

## 6.1. Measurement setup

An overview of the measurement setup is given in Figure 6.1.

A signal generator generated a square wave signal with an amplitude of  $0.7\text{ V}$  and  $0.45\text{ V}$ , respectively. As a square wave signal consists of several harmonics, the pre amplifier had to support a wide bandwidth.

The square wave of  $Ch1$  &  $\overline{Ch1}$  and  $Ch2$  &  $\overline{Ch2}$  of the AWG (arbitrary waveform generator) is amplified by broadband amplifier G1 and G2, respectively.

A DC bias voltage is applied to the inputs of the DUT to generate a square wave signal from  $V_{low} = -10\text{ V}$  to  $V_{high} = -5\text{ V}$ . The voltage swing of  $5\text{ V}$  as well as the DC bias voltage were needed to ensure that the input transistors switch completely on and off. Several power supplies provided the necessary DC supply voltages for the broadband amplifiers, bias tees and DUT.

For the measurement of the push-pull stage an attenuator with  $20\text{ dB}$  attenuation was connected between the output of the DUT and the input of the oscilloscope. This attenuator ensured that the specifications of the oscilloscope (scope 1) were complied.

The measurement of the voltage across the load capacitance was done by another oscilloscope (scope 2) which provides a handy probe. This probe allowed to measure the voltage

directly on the output line of the hybrid test circuit.

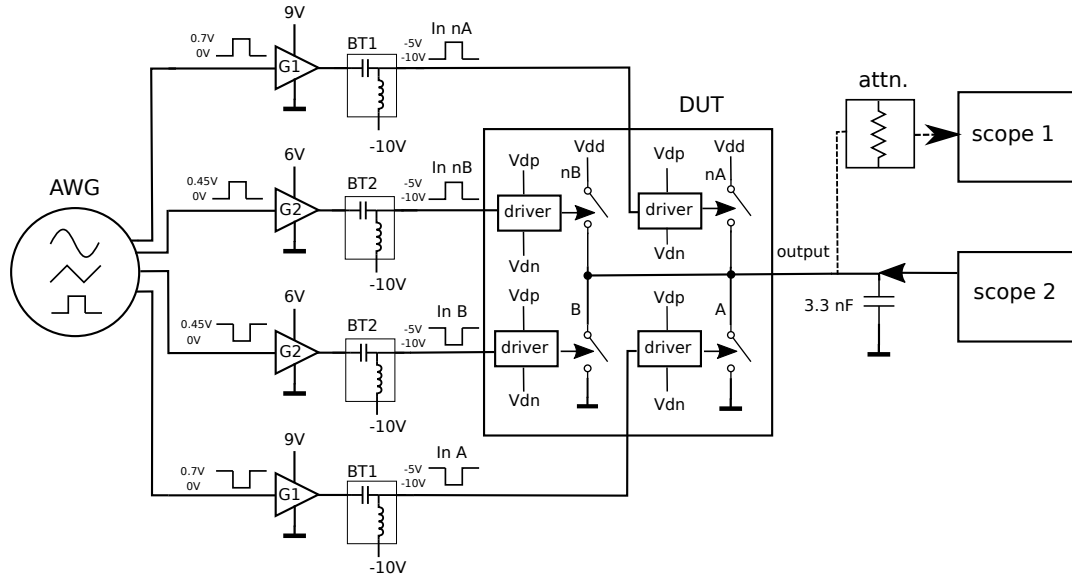


Fig. 6.1.: Schematic of time domain measurement setup

The elements of the measurement setup were:

- Signal generator: Keysight M8195A AWG
  - Ch1 &  $\overline{Ch1}$ :  $V_{p-p} = 0.7 \text{ V}$  (square wave)
  - Ch2 &  $\overline{Ch2}$ :  $V_{p-p} = 0.45 \text{ V}$  (square wave)
- Broadband Amplifier
  - G1: SHF803  
gain = 17 dB (typ.), B = 35 kHz - 40 GHz
  - G2: SHF804TL  
gain = 21 dB (typ.), B = 200 kHz - 55 GHz
- Bias Tee
  - BT1: SHF121A  
B = 50 kHz - 65 GHz
  - BT2: SHF121D  
B = 50 kHz - 65 GHz
- DUT
- Power supplies
- Attenuator: 18B50W  
B = DC - 18 GHz, Attenuation = 20 dB
- Capacitive load

ceramic SMD capacitor (3.3 nF)

- Oscilloscope
  - scope 1: DCA-X 86100D + 86118A (module)
  - scope 2: DSO-X 3034A + HP 10432A (probe)

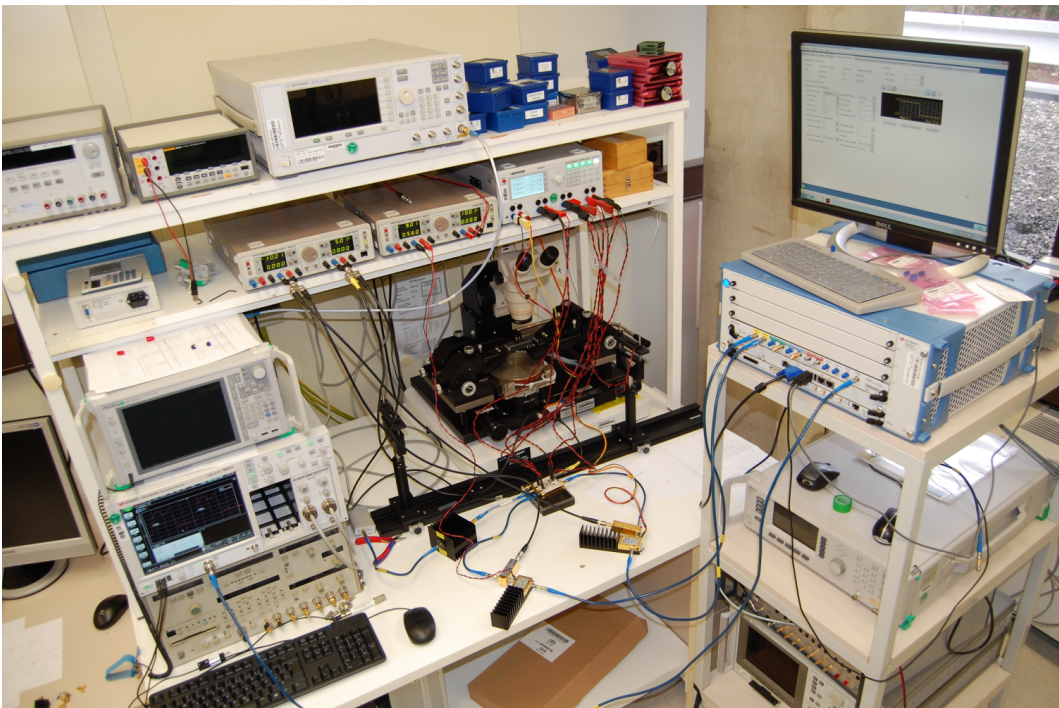


Fig. 6.2.: Photograph of measurement setup

## 6.2. Calibration and stability check

Before performing the first measurement the instruments and used devices had to be calibrated. The AWG output amplitude had to be adjusted to the proper value depending on which pre amplifier is used, as the broadband amplifier differ in their gain. The actual broadband amplifiers gain has to be checked as well as the proper configuration of the bias voltages. These prerequisites are necessary to ensure a proper measurement. After the calibration the first measurement checked the stability of the circuit. Therefore the DUT was supplied by its bias voltages and the current was checked if it stays constant. Due to the fact that the current was stabilized after the transient time, it showed that the circuit is stable. For this measurement the in- and output connectors were terminated with  $50\Omega$  terminations.

### 6.3. Time domain measurement of push-pull stage

After checking stability of the DUT a small signal is fed to its input. Feeding a square wave signal (digital signal) to the input of the device its output switches between  $V_{dd}$  and GND potential. This is done with the push-pull stage realized with multi chip assembling on a hybrid board. *The hybrid board consists of four inputs which two are working in differential mode.*

Switching the output to  $V_{dd}$  needed an in phase control signal. Two high side transistors should switch and feed the upper power rail which is  $V_{dd}$  to the output. Meaning both power transistors have to switch at the same time to provide  $V_{dd}$  to the output. While highside and lowside transistor both switched on the output is floating between  $V_{dd}$  and GND.

Figure 6.3 shows the square wave input control signal. The square wave signal form represents a digital signal with a data rate of 200Mbps while the fundamental analog frequency is at 100 MHz. The required peak to peak voltage is configured to be 0.7 V. The light grey signal represents one input stream while the darker grey signal represents the inverse one. This signal represents a digital bit stream which is needed to control the circuit. The data rate of the presented signal is 200 Mbps while the analog fundamental frequency is 100 MHz.

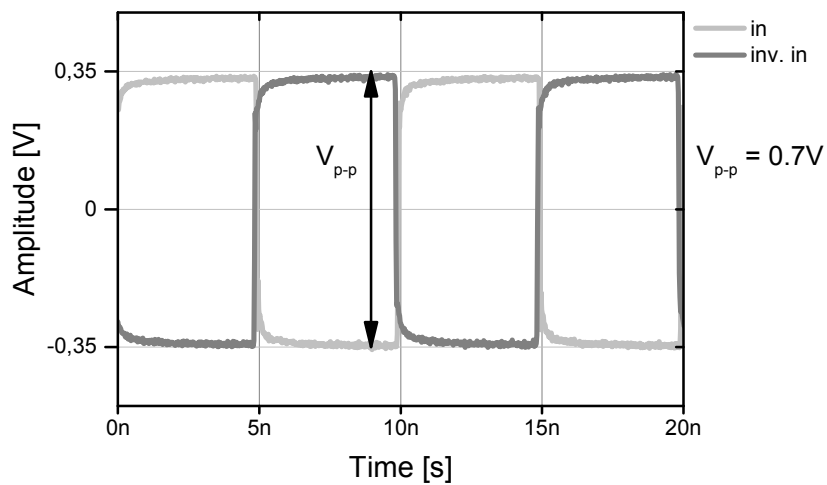


Fig. 6.3.: time domain measurement input control voltage

Using this input signal the circuit under test, with a  $50\Omega$  termination, provides the output shown in figure 6.4.

The light green signal is the measured data while the dashed line describes the ideal behaviour. In an ideal world there would be neither rising nor falling time and the signal would switch between logical one and zero.

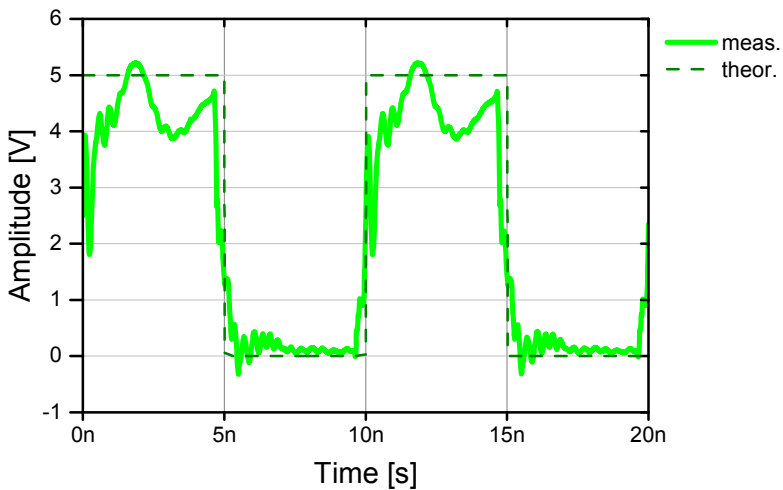


Fig. 6.4.: Time domain measurement of output voltage with 50 Ohm termination

This figure demonstrate the proper functioning of the presented output push-pull stage, as the signal switches between Vdd and GND. In addition to this it is demonstrated that the switches are very fast since the rising and falling edges are very steep. The frequency accords with the input signal shown in figure 6.3.

## 6.4. Time domain measurement of synthesized signal

The proper functioning of the designed circuit led to verifying that both bits work together. If both bits work concurrently, it is possible to synthesize a signal. This proofs the concept and the chosen approach. The two bit resolution restricts the output voltage waveform. In Figure 6.5 two different signals are shown which could be synthesized. The frequency of the synthesized triangular signal is 100 MHz while the voltage swing is 1.8 V and 0.8 V respectively.

The red signal represents a synthesized triangular waveform with a slope corresponding to  $3i_0$ , while the brown dashed signal provides the theoretical signal.

The blue signal represents a synthesized triangular waveform with a slope corresponding to  $1i_0$ , while the dashed darker blue signal provides the theoretical one.

The same notation is valid for the synthesized signal in figure 6.6. Here the signal frequency is 150 MHz which is the upper bound for this measurement setup. The signal integrity is much worse going beyond this frequency.

The difference between the slopes is getting smaller while the signal quality is decreasing.

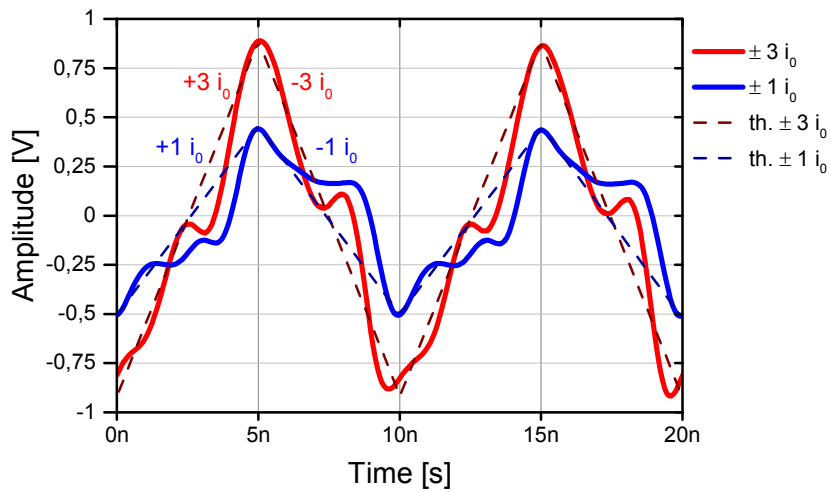


Fig. 6.5.: time domain measurement with capacitive load at  $f_s = 100\text{MHz}$

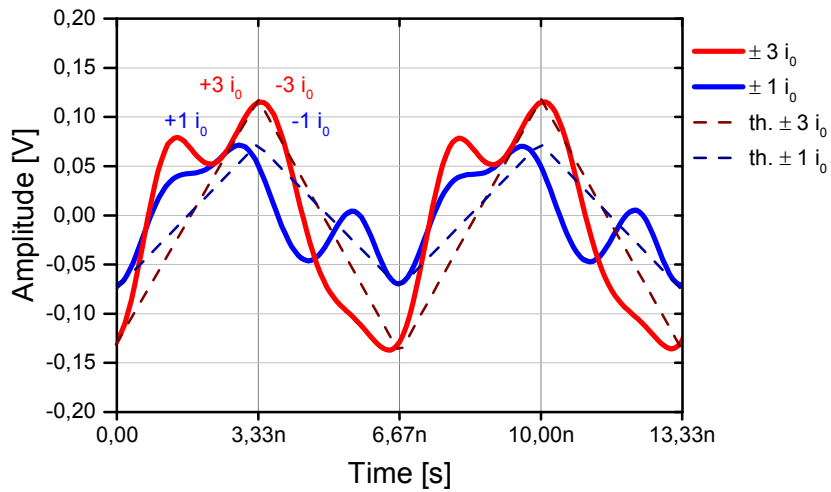


Fig. 6.6.: time domain measurement with capacitive load at  $f_s = 150\text{MHz}$

## 6.5. Discussion of measurement results

In a first step it was shown that the designed circuit converts a digital signal to an analog one. The frequency limit for this measurement setup consisting of this designed circuit is at roughly 150 MHz. Heat is critical. Aside from some parasitic effects the proof of the concept was successful.

## 7. Conclusions and outlook

The design and processing of a new MMIC structure containing the Riemann Pump was beyond the scope of this thesis.

The calculation of the Riemann Code have to be done with an external signal processor, which has to compute this code in real time. This could be a problem, since the energy consumption could increase and the real time calculation. In a more enhanced project a MATLAB algorithm would compute this code by minimizing the deviation between a theoretical signal and the synthesized signal.



# Bibliography

- [1] F. Rivet, Y. Deval, and B. D. Begueret J.-B., Dallet D., “A Software-Defined Radio based on Sampled Analog Signal Processing Dedicated to Digital Modulations,” in *Research in Microelectronics and Electronics Conference*, 2007, pp. 121 – 124.
- [2] Y. Deval, F. Rivet, Y. Veyrac, N. Regimbal, P. Garrec, R. Montigny, D. Belot, and T. Taris, “Full Software Radio Transceivers,” in *ASIC (ASICON), 2013 IEEE 10th International Conference*, 2013, pp. 1 – 4.
- [3] F. Rivet, Y. Deval, B. J.-B., D. Dallet, P. Cathelin, and D. Belot, “The Experimental Demonstration of a SASP-Based Full Software Radio Receiver,” in *IEEE Journal of Solid-State Circuits*, vol. 45, no. 5, 2010, pp. 979 – 988.
- [4] S. Grossman, “Software-defined radio poses major challenges for hardware and software developers,” *Defense Electronics*, 2005.
- [5] S. Maroldt, “Gallium Nitride Based Transistors for High-Efficiency Microwave Switch-Mode Amplifiers,” Ph.D. dissertation, Albert-Ludwigs Universität Freiburg im Breisgau, June 2010.
- [6] M. W. Chamberlain, “A software defined HF radio,” in *MILCOM 2005 - 2005 IEEE Military Communications Conference*, vol. 4, 2015, pp. 2448 – 2453.
- [7] C. Li, A. Raghunathan, and N. K. Jha, “An architecture for secure software defined radio,” in *Design, Automation & Test in Europe Conference & Exhibition*, 2009, pp. 448 – 453.
- [8] F. Rivet, F. Fadhuile, Y. Deval, and T. Taris, “Wide-Band Rejection of Interfering Signals,” in *IEEE 20th International Conference on Electronics, Circuits, and Systems (ICECS)*, 2013, pp. 767 – 770.
- [9] F. Rivet, Y. Deval, and B. J.-B. D. D. C. P. B. D., “A Disruptive Receiver Architecture Dedicated to Software-defined Radio,” in *IEEE Transactions on Circuits and Systems II: Express Briefs*, ser. 344 - 348, vol. 55, no. 4, 2008.
- [10] D. Y. Rivet F., “A 97mW 0-4GHz 65nm CCMOS Concurrent Receiver,” in *12th IEEE International Conference on Solid-State and Integrated Circuit Technology (ICSICT)*, 2014, pp. 1–3.

- [11] Y. Veyrac, F. Rivet, Y. Deval, D. Dallet, P. Garrec, and R. Montigny, “The Riemann Pump: a Concurrent Transmitter in Gan Technology,” in *21st IEEE International Conference on Electronics and Circuits and Systems (ICECS)*, 2014, pp. 594 – 597.
- [12] Y. Deval, F. Rivet, and Y. Veyrac, “Design by Mathematics of Full Software Radio circuits and systems: methodology and application to 5G standard,” in *EUROPEAN MICROWAVE WEEK*, 2015.
- [13] Y. Zhang, M. Rodríguez, and D. Maksimović, “100 MHz, 20 V, 90% efficient synchronous buck converter with integrated gate driver,” in *2014 IEEE Energy Conversion Congress and Exposition (ECCE)*, Sept 2014, pp. 3664–3671.
- [14] R. Quay, *Gallium Nitride Electronics*, ser. Springer Series in Materials Science; 96. Springer, Berlin, Heidelberg, New York, 2008, 469 S.
- [15] M. Seelmann-Eggebert, T. Merkle, F. van Raay, R. Quay, and M. Schlechtweg, “A systematic state ;space approach to large-signal transistor modeling,” *IEEE Transactions on Microwave Theory and Techniques*, vol. 55, no. 2, pp. 195–206, Feb 2007.
- [16] *Keysight Fundamentals of Arbitrary Waveform Generation, A high performance AWG primer, Reference Guide*, 4th ed., Keysight Technologies Deutschland GmbH, Herrenberger Str. 130 71034 Böblingen, Germany, June 2015.
- [17] N. Caka, M. Zabelli, M. Limani, and Q. Kabashi, “Impact of MOSFET parameters on its parasitic capacitances,” in *Proceedings of the 6th WSEAS Int. Conf. on Electronics, Hardware, Wireless and Optical Communications*, February 2007.
- [18] V. Carrubba, S. Maroldt, M. Musser, E. Ture, M. Dammann, F. van Raay, R. Quay, P. Brückner, and O. Ambacher, “High-Efficiency, High-Temperature Continuous Class-E Sub-Waveform Solution AlGaN/GaN Power Amplifier,” in *IEEE Microwave and Wireless Components Letters*, vol. 25, no. 8, 2015, pp. 526 – 528.
- [19] N. Deltimple, L. Leyssenne, E. Kerhervé, Y. Deval, and D. Belot, “Dynamic Biasing Techniques for RF Power Amplifier Linearity and Efficiency Improvement,” in *IEEE International Conference on Integrated Circuit Design and Technology*, 2010, pp. 232 – 235.
- [20] J. Everts, J. Das, V. den Keybus J., M. Germain, and J. Driesen, “GaN-Based Power Transistors for Future Power Electronic Converters,” in *IEEE Benelux Young Researchers Symposium (YRS2010) ,Leuven (Belgium)*, vol. 5, 2010.

- [21] I. S. Ghosh, U. Altmann, O. Kersten, M. Quibeldey, R. Follmann, P. Hildenhagen, M. Rittweger, L. Cabria, E. Cipriani, P. Colantonio, N. Aylon, and A. Chowdhary, “A 250 nm CMOS / LDMOS Pulse-Width Modulator and Driver for space-borne GaN switch mode power amplifiers in P-band,” in *11th European Radar Conference (EuRAD)*, 2014, pp. 356 – 359.
- [22] B. L. Gilmore R., *Practical RF Circuit Design for Modern Wireless Systems*. ARTECH HOUSE, Inc., 2003, vol. 2 Active Circuits and Systems.
- [23] M. P. van der Heijden and M. Acar, “A radio-frequency reconfigurable CMOS-GaN class-E Chireix power amplifier,” in *IEEE MTT-S International Microwave Symposium (IMS2014)*, 2014, pp. 1 – 4.
- [24] M. P. van der Heijden, M. Acar, and S. Maroldt, “A package-integrated 50W high-efficiency RF CMOS-GaN class-E power amplifier,” in *IEEE MTT-S International Microwave Symposium Digest (IMS)*, 2013, pp. 1 – 3.
- [25] M. P. van der Heijden, M. Acar, J. S. Vromans, and D. A. Calvillo-Cortes, “A 19W high-efficiency wide-band CMOS-GaN class-E Chireix RF outphasing power amplifier,” in *IEEE MTT-S International Microwave Symposium Digest (MTT)*, 2011, pp. 1 – 1.
- [26] Y.-P. Hong, K. Mukai, H. Gheidi, S. Shinjo, and P. M. Asbeck, “High efficiency GaN switching converter IC with bootstrap driver for envelope tracking applications,” in *IEEE Radio Frequency Integrated Circuits Symposium (RFIC)*, 2013.
- [27] C. Jarray, A. Bouabid, and B. Chibani, “Enabling and challenges for 5G Technologies,” in *World Congress on Information Technology and Computer Applications Congress (WCITCA)*, 2015, pp. 1 – 9.
- [28] S. Maroldt, P. Brückner, R. Quay, and O. Ambacher, “A microwave high-power GaN transistor with highly-integrated active digital switch-mode driver circuit,” in *IEEE MTT-S International Microwave Symposium (IMS2014)*, 2014, pp. 1 – 4.
- [29] S. Maroldt, C. Haupt, R. Kiefer, W. Bronner, S. Mueller, W. Benz, R. Quay, and O. Ambacher, “High Efficiency Digital GaN MMIC Power Amplifiers for Future Switch-Mode Based Mobile Communication Systems,” in *Annual IEEE Compound Semiconductor Integrated Circuit Symposium*, 2009, pp. 1 – 4.
- [30] S. Maroldt, R. Quay, C. Haupt, and O. Ambacher, “Broadband GaN-Based Switch-Mode Core MMICs with 20 W Output Power Operating at UHF,” in *IEEE Compound Semiconductor Integrated Circuit Symposium (CSICS)*, 2011, pp. 1 – 4.

- [31] Maroldt, S., R. Quay, C. Haupt, R. Kiefer, D. Wiegner, and O. Ambacher, “Integrated-Schottky-Diode GaN HFETs for High-Efficiency Digital PA MMICs at 2 GHz,” in *40th Microwave Conference (EuMC)*, 2010, pp. 636 – 639.
- [32] R. S. Pengelly, S. M. Wood, J. W. Milligan, S. T. Sheppard, and W. L. Pribble, “A Review of GaN on SiC High Electron-Mobility Power Transistors and MMICs,” in *IEEE Transactions on Microwave Theory and Techniques*, vol. 60, no. 6, 2012, pp. 1764 – 1783.
- [33] D. M. Pozar, *Microwave Engineering*, 4th ed. John Wiley & Sons, Inc., 2012.
- [34] R. Quay and S. Maroldt, “Design and modelling challenges for advanced class-S digital transmitters,” in *Workshop on Integrated Nonlinear Microwave and Millimetre-Wave Circuits (INMMIC)*, 2011, pp. 1 – 4.
- [35] U. Schmid, R. Reber, S. Chartier, W. Grabherr, R. Leberer, and M. Oppermann, “Advances on GaN based switch mode amplifiers for communication applications,” in *41st European Microwave Conference (EuMC)*, 2011, pp. 163 – 166.
- [36] Y. Veyrac, F. Rivet, Y. Deval, D. Dallet, P. Garrec, and R. Montigny, “A 65 nm CMOS DAC Based on a Differentiating Arbitrary Waveform Generator Architecture for 5G Handset Transmitter,” in *IEEE TRANSACTIONS ON CIRCUITS AND SYSTEMS - II: EXPRESS BRIEFS*, vol. 63, no. 1, 2016, pp. 104 – 108.
- [37] A. Wentzel, C. Meliani, and W. Heinrich, “A voltage-mode class-s power amplifier for the 450MHz band,” in *European Microwave Conference (EuMC)*, 2010.
- [38] D. M. Y. Zhang, M. Rodriguez, “High-Frequency Integrated Gate Drivers for Half-Bridge GaN Power Stage,” *Workshop on Control and Modeling for Power Electronics (COMPEL)*, 2015.
- [39] A. Zhang, L. Zhang, Z. Tang, X. Cheng, Y. Wang, K. J. Chen, and M. Chan, “Analytical Modeling of Capacitances for GaN HEMTs, Including Parasitic Components,” in *IEEE Transactions on Electron Devices*, vol. 61, no. 3, 2014, pp. 755 – 761.
- [40] S. Vitanov, V. Palankovski, S. Maroldt, and R. Quay, “Non-linearity of transconductance and source–gate resistance of HEMTs,” in *Proc. European Solid-State Device Research Conf. Fringe Poster Session*.

# **Appendix**

## **A. Schematic of the Riemann Pump circuit**

## B. Layout of the whole Riemann Pump circuit

bla bla bla bal bla lbal blalsl

bla bla bla bal bla lbal blalsl

**C. Photography of the realized Demonstrator  
version 1**

**D. Photography of the realized Demonstrator  
version 2**

bla bla bla bal bla lbal blalsl

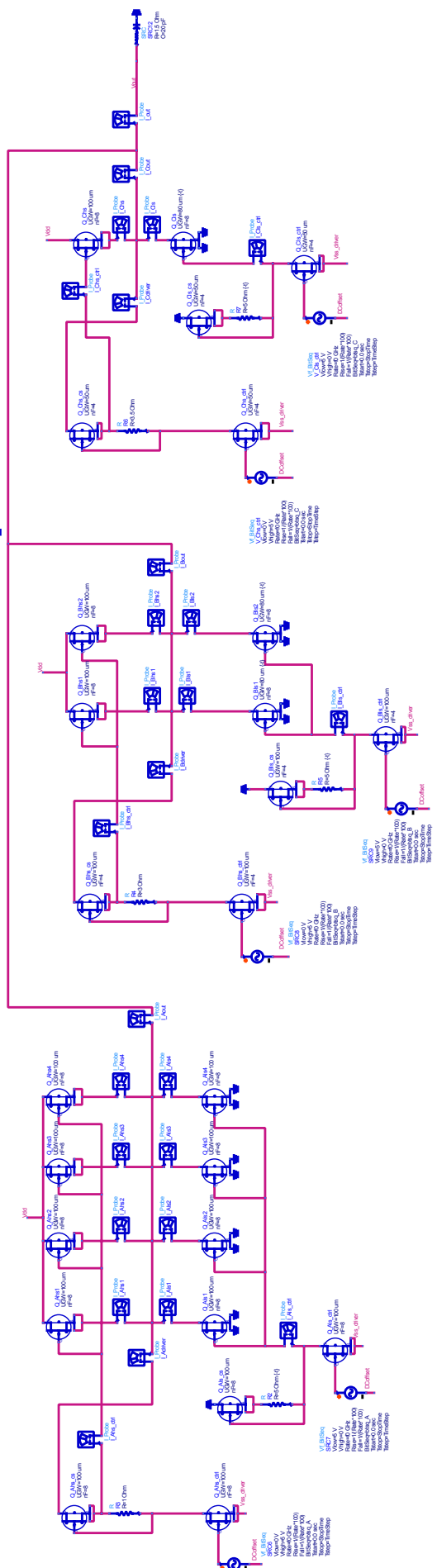


Fig. .1.: Realized circuit with ADS

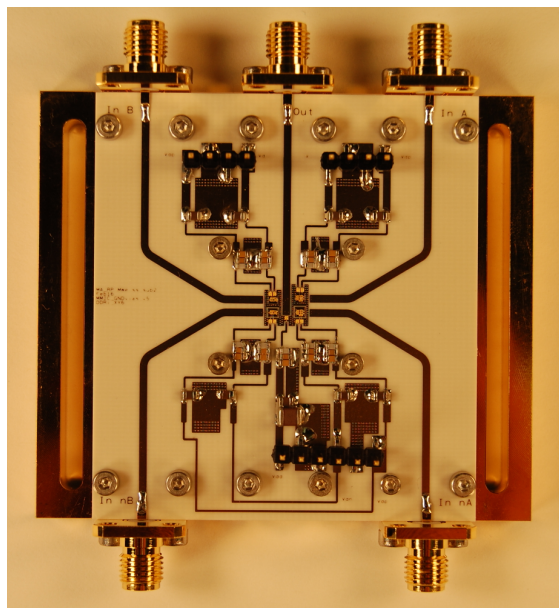


Fig. .2.: Photo demonstrator

